



Review

Terahertz fields and applications

D. Dragoman^{a,*}, M. Dragoman^b^a*Physics Department, University of Bucharest, P.O. Box MG-11, 76900 Bucharest, Romania*^b*National Institute of Microtechnology, P.O. Box 38-160, 72225 Bucharest, Romania*

Abstract

Terahertz signals were until recently an almost unexplored area of research due to the difficulties in generation and detection of electromagnetic fields at these wavelengths. Neither optical nor microwave techniques are directly applicable in the terahertz range since optical wavelengths are too short and microwave wavelengths are too long compared to terahertz field wavelengths. The development of ultrafast optical techniques, the manufacturing of semi-insulating semiconductors with very short lifetimes and of band-engineered heterostructures, as well as the micromachining techniques and nanotechnology have boosted the terahertz fields as a new area of research in quantum electronics with many important applications. The paper reviews the most recent results in THz fields and is focused on the physical principles of terahertz generators and receivers, underlining the link between terahertz devices and modern technologies such as micromachining and nanotechnology.

© 2003 Elsevier Ltd. All rights reserved.

Contents

1. Introduction	2
2. Terahertz field generation	6
2.1. Broadband THz generation	6
2.1.1. Broadband THz generation/detection using photoconductive effect	6
2.1.2. Broadband THz generation from semiconductor surfaces	21
2.1.3. Broadband THz generation using optical rectification	22

*Correspondence address. Department of Physics, University of Bucharest, P.O. Box 1-480, 70700 Bucharest, Romania. Tel./fax: +40-21-647-3382.

E-mail address: danieladragoman@yahoo.com (D. Dragoman).

2.1.4.	Broadband THz generation using nonlinear transmission lines	23
2.2.	Narrowband THz generation	25
2.2.1.	Narrowband THz generation based on photomixing	26
2.2.2.	Narrowband THz generation using optical parametric conversion	31
2.2.3.	Narrowband THz generation using electronic devices	32
2.2.4.	THz generation using semiconductor lasers, masers, tasers	33
2.3.	THz generation/detection using nanodevices	36
3.	THz propagation	43
4.	THz detection	49
4.1.	Detection of ultrashort electrical pulses	49
4.2.	CW THz heterodyne detection	51
4.3.	Direct THz detection using micro and nanodevices	54
5.	Terahertz main applications	57
6.	Conclusions	61
	References	61

1. Introduction

“Terahertz (THz) fields” is a generic term for waves with a spectrum between 0.1 and 10 THz. Although, strictly speaking, THz waves are those with frequencies between 1 and 10 THz the spectral range covered by the extended notion of THz fields includes some millimeter- and submillimeter-waves. Sometimes, especially in connection with imaging techniques, the THz spectrum is defined as T-ray. To get a better grasp of the frequency region we are referring to it is useful to mention that the frequency of 1 THz corresponds to a wavelength of 300 μm or 0.3 mm and to a wavenumber of 33 cm^{-1} . THz fields have wavelengths extending from 3 mm (0.1 THz or 100 GHz) up to 30 μm (10 THz); this wavelength interval ranges between the top edge of the millimeter wave spectrum to the bottom edge of the optical spectrum corresponding to the boundary of the far-infrared (FIR) spectral region.

The location of the THz field spectrum between the electronic and photonic domains implies that optical or electronic, or even better a mixture of optical and electronic means, can be employed for THz field generation, detection and processing. For example, THz fields can be generated with the help of a down-conversion optical process or a photoconductive process, THz fields propagate into free space using an antenna or are guided through a microwave-type waveguide such as the coplanar wave waveguide (CPW), and so on. However, there are also all-optical or all-electronic means to produce or receive THz fields; lasers or electronic oscillators or multipliers are such examples.

The multidisciplinary character of the research area dealing with THz fields, implied by their spectral location between frequency ranges covered by well-developed and still separately developing research areas, requires a deep knowledge of optics and photonics, microwave engineering and semiconductor physics. The multidisciplinary character of the research in THz fields resides not only in the disciplines that constitute its foundation, but also in the impressive areas of applications, which includes astrophysics, plasma physics, spectroscopy, medical imaging, biology, and communications.

Despite the fact that THz technology is at the boundaries of microwave and photonic technology (or because of it), it is quite underdeveloped compared with the achievements in microwave or photonics. There are very few commercially available instruments for the THz frequency region and very often they lack the precision required for performing accurate measurements. An illustrative example of this regrettable state of affairs is that the highest oscillation frequency obtained at room temperature using an electronic device such as an InAs/AlSb resonant tunneling diode, which is 0.712 THz [1], was measured with an estimated error of 50% (the emitted power is 0.3 μ W). There are also no miniaturized and low-cost THz sources.

Although the value of 0.712 THz mentioned above is the highest performance ever obtained with a single electronic device, ballistic transistors with a cutoff frequency of several THz were recently reported; one should be optimistic that a single electronic device will be able soon to oscillate at THz frequencies and provide an output power greater than some mW [2]. Another promising direction of research towards powerful THz sources involves wide bandgap semiconductors, which are able to increase significantly the output power and the cutoff frequency of negative differential resistance devices due to an increased electrical strength. In this respect, GaN Gunn diodes are expected to oscillate at 740 GHz and even up to 4 THz. Wide bandgap semiconductors can be used also in multipliers designed to generate THz frequencies with a significant output power (0.1–1 mW); simulations show that a single GaN Gunn diode can deliver 10 W at about 200 GHz [3].

Heterostructure semiconductor lasers based on interband transitions between conduction and valence bands—one of the most popular laser sources in the visible and near infrared spectral range—cannot extend their operation into the FIR or THz range. In these lasers, called ambipolar semiconductor lasers because both electrons and holes are involved in transitions, the energy of the generated radiation is of the order of the bandgap, i.e. on the order of 1 eV. On the other hand, lasing at THz corresponds to a difference in the energy levels involved in transition of about 4 meV, much smaller than the bandgap in semiconductor materials. Therefore, new physical principles must be used for lasing at frequencies in the FIR or THz ranges. One possible solution is to employ transitions between discrete levels or subbands situated either in the conduction or the valence band, separated by much smaller energy gaps than the bandgap in semiconductor materials. These intraband transitions involve only one carrier type, the lasers based on them being called unipolar lasers. By abandoning the ambipolar laser in favor of the unipolar laser the mechanism for population inversion must be also changed: the electrical injection common for ambipolar lasers is replaced by tunneling. These quantum tunneling

lasers demonstrated good performances first in the FIR when cooled, and nowadays at THz frequencies near room temperature. Based on these principles a quantum cascade laser generated more than 2 mW output power at 4.4 THz at a temperature of 60 K [4]. This is an impressive achievement, although the working temperature is still low. The main effort of many research teams is a room temperature THz laser; such a laser may become reality sooner than it is expected.

Although there are encouraging perspectives regarding an electronic or photonic single device able to generate THz signals at room temperature, THz continuous-wave (CW) sources are a rarity and are not miniaturized, requiring very expensive components. Free-electron lasers (only a small number are working in the world!), IR-pumped gas lasers (commercially available), or electronic tubes are the only THz sources that provide output powers greater than 1 mW [5]. Moreover, these CW THz sources are bulky, quite expensive and only few companies are producing them. Therefore, many THz sources used in the laboratory are not of the CW type, being based on short electrical pulses with picosecond (ps) or sub-ps duration and obtained from photoconductive, rectification or other optical mechanisms when a femtosecond (fs) laser excites a semiconductor material. High power THz pulses with a radiated peak power exceeding several hundreds of W can be obtained from these pulsed lasers at fs excitation, although the devices are very expensive [6]. So, in the THz range of frequencies we are confronted with a huge disadvantage: the inexistence of miniaturized devices working at room temperature able to generate CW THz fields with a relatively high output power.

The situation is much better for THz receivers. In the latest years very sensitive, low noise, room temperature integrated receivers based on Schottky diodes were demonstrated. However, these receivers must be pumped with a local oscillator (LO), which should have a power exceeding 0.1 mW, requirement that is presently satisfied only by an IR pumped gas laser or by electronic multipliers. The weird situation arises that, in the case of THz Schottky receivers, the mixer is miniaturized, but not the LO. If we want better noise performances cooled THz receivers such as hot-electron bolometer (HEB) mixers are used, which require a LO with a power smaller with 3–4 orders of magnitudes compared to that pumped in a THz Schottky mixer. In this case, a fully integrated THz receiver could be possible, since a tunable THz LO with a power average of 1 μ W is achievable using existing integrated electronic or photonic technologies. The price paid is the working temperature of the receiver, which is not greater than a few K since in these receivers the Schottky diodes are replaced with superconducting junctions or bolometers based on nano-sized metal films. So, the receiver must be introduced inside a bulky and well-controlled cooling system. The type of receiver depends on the specific THz application. For example, in astrophysics a cooled receiver is a must since the astronomical sources are very weak and accompanied by noise. On the contrary, if we intend to use a THz receiver for spectroscopy or imaging we need a compact and even portable system so an uncooled receiver is desirable.

The THz technology needs also many passive devices such as lenses, waveguides, beam-splitters and antennas. The most common material for their realization is presently the high-resistivity Si since at THz frequencies this material is practically

transparent, the absorption coefficient being of the order of only 0.04 cm^{-1} , and has an almost constant index of refraction of 3.42 [7]. This fact is of the considerable interest for THz devices since Si technology is the most advanced and developed semiconductor technology in the world and thus advanced technologies developed for Si, such as MEMS fabrication techniques, can be successfully used to satisfy the quite tight tolerances required for THz passive devices. Especially MEMS processing techniques applied to THz devices have a very low costs compared with any other THz technologies, and ensure an increased flexibility and complexity. Moreover, using the 3D micromachining of Si, passive as well as active devices can be integrated in a single THz circuit [8,9]. However, the best solution would be to base the THz technology on Si for passive devices and integrate them with active devices based on III–V semiconductor compounds or wide bandgap semiconductors.

The review will analyze the main methods and technologies for THz generation, detection and processing. On the other hand, the most stringent problem for THz technology is the quest for a CW THz source with reduced or even miniaturized size able to generate a power greater than 1 mW. Therefore, a large part of the paper will be devoted to the description of the main methods for THz field generation based on either photonic or electronic means, or on a combination of them. Then, the paper will present the major results concerning the propagation of THz fields. The detection of THz fields will be reviewed and the last part of the paper will be dedicated to THz applications. A simple enumeration of the emission/detection methods for THz fields would certainly not deserve too much attention so that we will focus our analysis of THz emitters/detectors on the physical principles and effects on which THz emitters and detectors are based. An unexpected richness of physical principles and effects are revealed, starting with the basic quantum interference on which these devices are based on.

It is obvious from the above presentation that the THz technology has not yet reached maturity and a lot of work remains to be done to improve the performances of the existing devices in the THz range. The interest in the THz frequency range is fuelled by the fact that this range of frequencies is the place where unique physical phenomena with characteristic features are produced. Some of these unique features are listed below.

- The spectral energy distribution in observable galaxies shows that 50% of the total luminosity and 98% of photons emitted since Big-Bang are located in the THz frequency range [5].
- THz fields interact strongly with polar substances but penetrate those non-polar. Thus, the absorption spectra of many polar molecules, for example H_2O , C, N_2 , O_2 , O_3 , HCl, CO, SO_2 , CH_3CN , etc., have many and distinct spectral peaks in the THz range. This unique signature of molecules in the THz range is of highest importance in monitoring the surrounding medium, air pollution detection, or gas sensing.
- Biological tissues or other biological constituents have distinct signatures in the THz range. For example, DNA signature, DNA manipulation, gene diagnostics were demonstrated experimentally using THz techniques [10].

- Very small/miniaturized antenna arrays and circuits can be used in the THz range since the corresponding wavelengths, which impose the dimensions of antenna and circuits are much smaller than those encountered in the microwave and millimeter-wave spectral intervals. This advantage is of great importance in medical imaging and imaging devices such as THz cameras. Moreover, despite their reduced size, THz devices are able to send or receive a huge quantity of information that can be encoded in the ultra wideband of THz signals.
- THz signals are the information carriers in the 1–10 Tb/s optical communications systems, which are developed now and are expected to become a commercial reality in the next decade. THz modulators able to modulate ultrafast laser diodes will use quantum devices such as ballistic diodes or transistors with a cutoff frequency well beyond 10 THz.
- The 1 ps switching performance of the THz transistor is studied now by leading companies using the latest discoveries in nanotechnology [11]. For example, the dimension of the gate of this transistor is 90 nm thick (about 5 atomic layers) and a SRAM cell based on it is smaller than $1 \mu\text{m}^2$. If the power consumption problems occurring at such huge data speed will be solved, a computer will run at a speed that is unimaginable today making possible, for example, real-time speech recognition and translation.

It is now clear that THz technology age will come soon, since the THz features mentioned above are indeed tremendous and imply astonishing applications in various areas of science such as astronomy, biology, computers and communications.

2. Terahertz field generation

2.1. Broadband THz generation

The common feature of the next paragraphs is the quest for the production of an ultrashort electrical pulse with durations within the interval 0.2–2 ps, which has a spectrum inside the THz range. The generation of this ultrashort electrical pulse could be accomplished by mixed optical and electronic means (see THz photoconductive devices), using only optical means (see THz generation using optical rectification) or using only electronic means (nonlinear transmission lines).

2.1.1. Broadband THz generation/detection using photoconductive effect

Rapid (ps) photoconductors have been used in the last two decades to generate ultrashort electrical signals with duration of several hundreds of fs that have a spectrum situated in the THz region. Nowadays, this is the most encountered method to generate/detect THz fields.

When a fs laser with an intensity $I(t)$ excites a biased semiconductor with photon energies greater than its bandgap electrons and holes are produced at the illumination point in the conduction and valence bands, respectively. The rapid

changes of the photocarriers' density and their acceleration due to the applied dc bias V_b produce an electromagnetic field radiating into free-space with the help of an antenna. The production of ultrashort currents with a full-width half-maximum (FWHM) of 1 ps or less strongly depends on the carrier lifetime in the semiconductor. Although intrinsic semiconductors have a carrier lifetime exceeding hundreds of ps, some processing techniques such as annealing, ion implantation, and radiation exposure, allows the reduction of the carrier lifetimes to sub-ps duration. This category of semiconductors is referred to as semi-insulating semiconductors. An updated review of semi-insulating semiconductors and their applications in optoelectronics can be found in Ref. [12]. Nowadays, the most exploited semiconductor with a very short carrier lifetime is the low-temperature grown GaAs (LT-GaAs) that has a photocarrier lifetime of $\tau_t = (\tau_e + \tau_h)/2 = 0.25$ ps, where $\tau_e = 0.1$ ps and $\tau_h = 0.4$ ps are the lifetimes of electrons and holes, respectively. Throughout this paper the subscripts e and h refer respectively to electron and hole. LT-GaAs has also a quite high mobility (10^3 cm²/V s) and a high breakdown field (10^5 V/cm).

So, the rapid biased photoconductor excited by a fs optical pulse (pump beam) plays the role of a transient current source, which feeds an antenna propagating into space transients with a short time duration. To detect such transients a device similar to the one that emits them is needed, but the photodetector is no longer biased. The current I_{out} is detected at the photoconductor pads when excited by a fs optical pulse replica of that used at the emission point (probe beam). This optical pulse with an intensity $I(t + \tau)$ is subjected to a variable delay line that delays it with τ compared to the excitation pulse $I(t)$. The generation/detection principle of THz fields based on the photoconductive effect is represented in Fig. 1.

Initially, photoconductors were used to feed nearby antennas and produce transients with a few ps duration [13]. Then, the antenna was integrated on the same substrate with the photoconductor, the device that resulted being called photoconductive antenna or Auston switch [14]. The integration of antenna and photoconductor on the same substrate, combined with the search of semi-insulating semiconductor materials with very short carrier lifetimes such as radiation damaged silicon on sapphire (SOS), InP bombarded with He ions and later LT-GaAs resulted

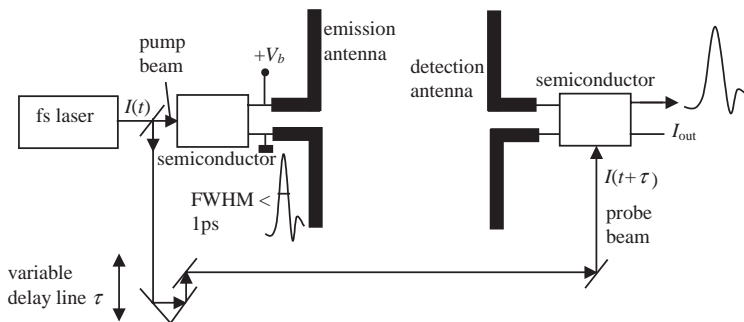


Fig. 1. Schematic representation of generation/detection of THz fields using the photoconducting effect.

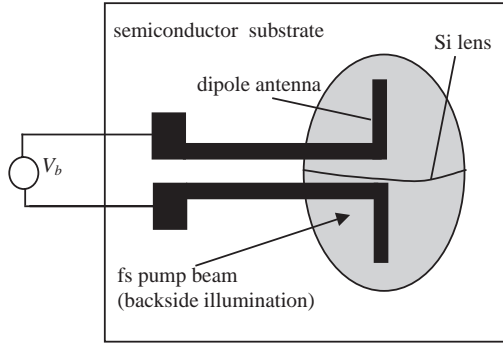


Fig. 2. Auston switch.

in the generation of electrical pulses with sub-ps duration, which extended the spectral response of the photoconductive antennas in the range 0.1–3 THz. A review on initial researches focused on the development of THz photoconductive sources can be found in Ref. [15]. One version of the Auston switch is presented in Fig. 2 and consists of a coplanar-stripline (CPS) terminated with a dipole antenna metallized on the semiconductor substrate and having two arms with lengths of about 40 μm . A Si spherical lens is mounted above the antenna to collimate the emitted THz radiation.

The free carrier lifetime in a photoconductive antenna on a LT-GaAs semiconductor can be approximated as equal to the carrier trapping time because the trapping time in mid-gap states that trap the photocarriers is much shorter than the recombination time between electrons and holes [16].

In these conditions, the carrier density behavior in time is given by

$$dn/dt = -n/\tau_t + G(t), \quad (1)$$

where n is the carrier density and $G(t) = n_0 \exp(t/\Delta t)^2$ is the generation rate of carriers due to laser pulse excitation, with Δt the laser pulse width that can be chosen in the interval 30–150 fs and n_0 the generated carrier density at $t = 0$. The carrier lifetime τ_t can be engineered to take values in the interval 0.1–5 ps by modifying the annealing temperature for LT-GaAs containing different excess arsenic concentrations [12]. The generated carriers are accelerated by the electric field bias with a velocity rate given by

$$dv_{e,h}/dt = -v_{e,h}/\tau_{rel} + (q_{e,h}E)/m_{eff,e,h}, \quad (2)$$

where $v_{e,h}$ are the average velocity of the carriers, $q_{e,h}$ is the charge of the electron or hole, τ_{rel} is the momentum relaxation time (equal to 30 fs in LT-GaAs), and E is the local electric field, which is less than the applied bias E_b due to the screening effect of space charges. More precisely,

$$E = E_b - P/3\epsilon_r, \quad (3)$$

where ϵ_r is the dielectric constant and P the polarization induced by the separation of electrons and holes. The polarization depends on time according to the

expression

$$dP/dt = -P/\tau_{\text{rec}} + J, \quad (4)$$

where τ_{rec} is the recombination time between electrons and holes ($\tau_{\text{rec}} = 10$ ps for LT-GaAs) and $J = env_h + (-e)nv_e$ is the current density.

The far-field radiation is given by

$$E_{\text{THz}} \propto \partial J / \partial t \propto ev \partial n / \partial t + en \partial v / \partial t, \quad (5)$$

where $v = v_e - v_h$. The transient electromagnetic field E_{THz} consists of two terms: the first term describes the carrier density charge effect while the second term describes the effect of charge acceleration due to the electric field bias. Detailed simulations have been carried out in Ref. [16] regarding Eqs. (2.1.1.1)–(2.1.1.5). The main results can be summarized as follows:

- (i) E_{THz} is proportional to the inverse of effective mass of the carriers. Since in LT-GaAs the effective mass of the hole is five times larger than that of the electron, the effect of holes in the THz radiation is significantly reduced compared to that of electrons but cannot be ignored due to the screening effect.
- (ii) The first term in Eq. (2.1.1.5) [16] is much greater than the second so that the THz radiation is produced mainly due to the ultrafast change of the carrier density $v \partial n / \partial t$, while the effect of carrier acceleration has a smaller effect.
- (iii) The pulse width of E_{THz} becomes larger when the width of the excitation laser pulse is increased.
- (iv) E_{THz} is a dynamic bias when the photoconductive antenna works as a detector. The detector acts like a filter, filtering only the shortest wavelength components of the transient electric field. The radiated THz field is thus considerably distorted.

So, THz Auston switch performances depend on: (i) the optical pulse duration, (ii) the semiconductor substrates which must have a very short carrier lifetime and a high mobility, and (iii) the antenna geometry.

This last dependence has received a great deal of attention; Auston switches were made with a multitude of antenna geometries such as Hertzian dipoles, resonant dipoles, dual dipoles, slot antennas, tapered endfire antennas, log-periodic antennas, etc. In Fig. 3 we present the dependence of the electrical pulse duration of the transient current measured between two consecutive peaks (either positive or negative) on the length L of the dipole. A linear decrease of the electrical pulse duration is observed with the reduction of the dipole length. Since the geometry of the antenna is so important for THz radiation we have presented in Fig. 4 some of the most commonly encountered THz planar antennas. They are divided into two large categories depending on the direction of the radiation pattern: antennas (a)–(d) are named broadside antennas and are radiating in a direction perpendicular to the substrate (\perp) while antennas (e)–(h) are named endfire antennas, radiating in a direction parallel to the substrate (\parallel).

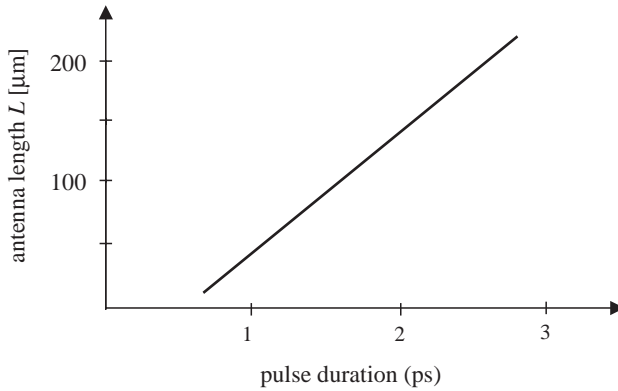


Fig. 3. Antenna length dependence on pulse duration.

The surface impedance of the metal from which all THz antennas are made is given by

$$Z_s = [i\omega\mu_0(1 + i\omega\tau)/\sigma_0]^{1/2} = (1/2)(\mu_0/\tau\sigma_0) + i\omega(\tau\mu_0/\sigma_0) = R_s + iX_s, \quad (6)$$

where σ_0 is the dc conductivity, τ is the collision or relaxation time of electrons in the metal and ω is the frequency. At microwave frequencies $\omega\tau \ll 1$ and the formula above is transformed into the formula that describes the well-known skin effect, the imaginary part of the surface impedance being negligible. On the contrary, in FIR and IR the complex part (reactance) of the surface impedance can be no longer neglected and plays a major role in establishing the performance of antennas since it increases linearly with the frequency while the real part of Z_s is remaining constant. R_s does not exceed some ohms, whereas X_s varies between 10 and 60 Ω for the wavelengths in the range 1–70 μm . The X_s increase affects the performances of antenna in several ways [17]. First, there are no longer orthogonal modes and homogeneous boundary conditions in any radiating structure and the method of separation of variables is no longer valid in many cases. This means that the simulation results for THz antenna must be treated with extreme care, since the effect of the surface impedance cannot be precisely taken into account in most of the cases. If we consider a simple transmission line model applicable for dipoles or bowtie (biconical) lines, the effect of the surface impedance is to slow down the propagation constant with a factor $\Delta\beta = (X/2)(C/L)^{1/2}$, where C and L are the capacitance and inductance per unit lengths, respectively. This slowing down can destroy the main beam of traveling-wave antennas of the types presented in Fig. 4.

Unfortunately, in the case of THz antennas not only the metal, but also the thickness of the substrate t has dramatic consequences on the performances. In microwave circuits $t \ll \lambda$, relation that guarantees the cancellation of substrate modes, which has as a result the reduction of the radiation and the dielectric losses. On the contrary, at THz and IR frequencies this inequality is no longer valid and very often the substrate thickness well exceeds the wavelength: $t \geq \lambda$. As a consequence the energy generated above a critical angle is trapped in the semiconductor substrate due

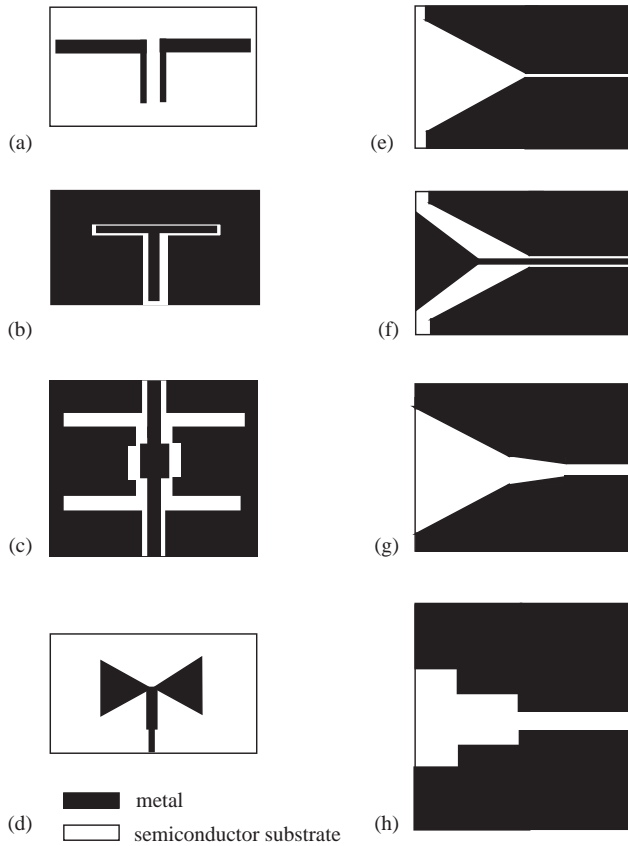


Fig. 4. THz antennas. (a)–(d) broadside antennas: (a) dipole, (b) single-folded slot, (c) double-folded slot, (d) bowtie; (e)–(h) endfire antennas: (e) Vivaldi, (f) slot V antenna, (g, h) tapered slot.

to the occurrence of substrate modes. Depending on the antenna thickness it is possible that a large part of the radiated power (more than 90% in some situations) is trapped into the substrate. Therefore, small losses can only be obtained when THz antennas and propagating structures working at THz are patterned on very thin substrates. For example, the substrate thickness must be smaller than 0.04λ for a slot antenna and smaller than $0.01\lambda_0$ in the case of dipole antennas [18]. This means that we need a substrate thickness less than $3\ \mu\text{m}$. This amazing achievement was possible only in the last years using the micromachining techniques borrowed from MEMS technology and adapted for the semi-insulating semiconductors. Even using these thin substrates, a dielectric layer over the antenna is still needed to collimate the THz radiation. This dielectric has a semispherical shape playing the role of lens also preventing the refraction of waves emerging from the antenna at the dielectric-air interface. A similar constraint regarding the thickness of the substrate exists for endfire antennas. In this case, we have $0.005 < [(e_r)^{1/2} - 1]t/\lambda < 0.03$ giving also thicknesses of few microns at THz frequencies.

The physical characteristics mentioned above are common for all antennas from Fig. 4. However, their performances are quite different. Some of them show a resonant behavior around a certain frequency and are therefore termed resonant antennas. This is the case of the dipole and of the single- and double-folded slot antennas. The dipole antennas are not compatible with CPW lines; the CPW line is the standard configuration of the transmission lines in millimeter waves and THz integrated circuits. In this type of antennas the radiation is coupled into the substrate beyond the resonance. On the contrary, the resonant single-folded and double-folded slot antennas are compatible with CPW lines and have an extended ground plane shielding the dielectric from the free-space. Therefore, they are very frequently used in the THz region. Moreover, they show a radiation pattern with a main symmetric lobe and with secondary lobes situated at a moderate level (-15 to -20 dB) [19]. In contrast with the narrow band antennas mentioned above, the broadband bowtie antenna can be easily matched in a large range of frequency. It has a radiation pattern consisting of two main lobes, which is its main disadvantage. This disadvantage can, however, be overcome by positioning a silicon lens off the symmetry axis of the antenna. In this way the radiation pattern shape is transformed from a bi-lobed to a single lobe at the expense of a 3 dB reduction of the radiated power. Due to its large bandwidth, it was experimentally proven that the detected THz signal produced by a bowtie is greater with 26 dB than that produced by slot antennas [20]. The endfire antennas are also broadband and have medium gain values that can be increased by increasing the length of the antenna. Some of them, like the Vivaldi antenna, cannot be directly excited with CPW lines, but with balanced two-wires transmission lines like CPS. These antennas need a balun to match them to a CPW line at the expense of losing 3 dB of power. Since the endfire antennas are not located on the same axis with the lens, additional integration problems will be encountered. A review regarding the properties of endfire antennas can be found in Ref. [21]. A recent photoconductive antenna configuration able to radiate efficiently THz fields is based on the singularities of the electric fields that occur at the tips of sharp metallic electrodes [22]. Its configuration is presented in Fig. 5. This antenna was able to emit an average THz power of $3 \mu\text{W}$ under a 20 mW optical excitation using a $45 \mu\text{m}$ dipole length; this power is one order of magnitude greater than that emitted by other photoconductive antennas. High average THz powers are obtained using metallic dipole antennas supported on InAs substrates. In

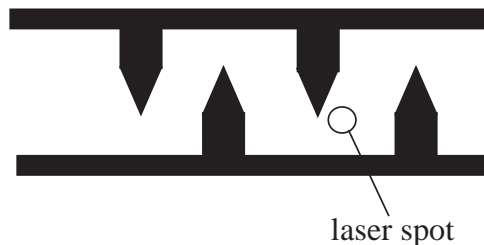


Fig. 5. The singular electric field THz photoconducting antenna.

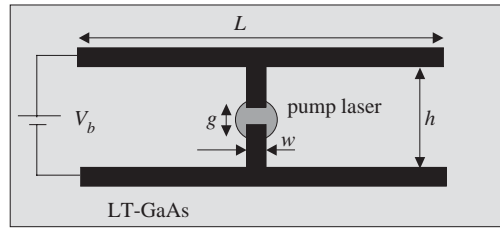


Fig. 6. CPS dipole antenna.

this case, an average power of 650 μW was obtained placing the antenna in a 1.7 T magnetic field and illuminating it with 1.5 W ultrashort pulses [23].

A CPS dipole antenna is also able to emit high THz powers in an ultrawide bandwidth of 40 THz. Its configuration is displayed in Fig. 6 [24]. Typical values for the antenna configuration are $g = 5\text{--}10\ \mu\text{m}$, $w = 10\text{--}20\ \mu\text{m}$, $h = 30\text{--}50\ \mu\text{m}$, $L = 1\ \text{mm}$. The peak value of the THz field is given by

$$E_{\text{THz}}^{\text{peak}} = e\mu\tau_{\text{int}}[(1 - R)/hf](P_{\text{in}}/g)(V_b/g), \quad (7)$$

where τ_{int} is the interval between pump pulses, μ is the mobility of the carriers, R is the reflection coefficient of the substrate, hf is the photon energy of the pump laser of frequency f and P_{in} is the average power of the pump laser. A high value of $E_{\text{THz}}^{\text{peak}}$ is obtained if the substrate has a high mobility and a high resistivity, requirements that enable the application of high bias values V_b . These criteria are satisfied by LT-GaAs. The peak value $E_{\text{THz}}^{\text{peak}}$ does not increase indefinitely, but saturates at a certain intensity, I_0 , or power, P_0 . We have

$$E_{\text{THz}}^{\text{peak}} \propto P_{\text{in}}/(P_0 + P_{\text{in}}) \propto g(P_{\text{in}}/A)/(I_0 + P_{\text{in}}/A), \quad (8)$$

where the illuminated area A is proportional to g^2 . From the above relation it follows that to obtain a maximum $E_{\text{THz}}^{\text{peak}}$ it is necessary to adjust the gap value so that the pump intensity P_{in}/A equals the saturation intensity.

As we have mentioned above, THz antennas are almost always accompanied by lenses, which cover them. When the lenses are made from the same material as the antenna substrate they are sometimes termed substrate lenses. There are two main types of substrate lenses: hemispherical and hyperhemispherical. Initially, these substrate lenses have been used as a semi-infinite antenna dielectric substrate, which eliminates the substrate modes. Since the substrate lenses also increase the gain of antennas, the lenses accompany THz antennas even when they are realized on very thin substrates. The first type of lens that appeared—the hemispherical lens—was used as a collimating lens, the THz antenna or THz antenna array being positioned in its focus. Although, the rays emerging from this lens are collimated, there are also rays that are trapped inside the substrate lens due to the total internal reflection, which occurs at large angles. The net effect is the wave-front aberration that is unavoidable for this type of lenses. The distance between the emitter and the lens tip is

$$d_{\text{emitter-lens}} = Rn/(n - 1). \quad (9)$$

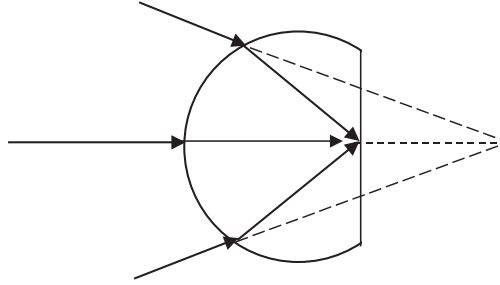


Fig. 7. Hyperhemispherical lens. The dashed lines represent the path of the rays in the absence of the lens.

In the case of a Si hemisphere lens this distance is $1.41R$, where R is typically 3–4 mm.

The second important substrate lens configuration is the hyperhemispherical substrate lens, which is displayed in Fig. 7. It was designed to reduce the disadvantages of the hemispherical substrate lens: there are no internal reflections in the case of hyperhemispherical lens. Since the rays are no longer totally reflected there is no wave-front aberration. The hyperhemispherical lens is an aplanatic lens, which reduces the beamwidth of the radiation pattern of antennas and increases the antenna gain by n^2 , where n is the dielectric constant of the substrate and the lens. The distance between the THz antenna and the hyperhemispherical lens is given by

$$d_{\text{emitter-lens}} = R(n + 1)/n. \quad (10)$$

This distance is $1.3R$ for a Si hyperhemispherical lens.

Many THz antenna arrays used for imaging or for receiving purposes were designed with substrate lenses. Bowtie antenna arrays, Yagi-Uda arrays, CPW slot antennas, single- and double-folded slot antennas are among them. For a review of THz lenses properties and applications see Refs. [18,25,26]. A comparison between the two main types of substrate lenses was recently made by Ref. [27]. It was found that the directivity of the collimating lens, defined as $D = 2 \max |E(\theta)|^2 / \int |E(\theta)|^2 \sin \theta d\theta$, increases with frequency and is about 30 dB at 1 THz, which means that the majority of THz energy is propagating in a beam with a width of a few degrees. In deep contrast, the directivity of the hyperhemispherical lens is quite low and independent of frequency; it has a value of about 3 dB at 1 THz, the THz energy propagating in this case in a beam with a width of about 30° . However, the hyperhemispherical lens couples much better to a gaussian mode. While the collimating lens has no effect on the bandwidth of the THz emitted signal, this bandwidth is dramatically restrained in the case of the hyperhemispherical lens. In the last case diffraction and interference fringes have been detected even in a broadside direction.

Although an optimized photoconductive antenna incorporates many innovative ideas regarding the substrate, antenna, or lenses, the THz generation based on the photoconductive effect shows a poor efficiency, i.e. ultrashort pulses with a power of

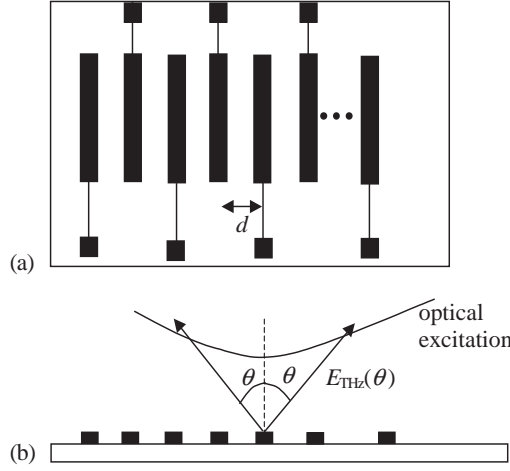


Fig. 8. THz photoconducting array. (a) Schematic representation, and (b) emitted field.

tens of mW are transformed in THz signals with a power not exceeding a few μW . In what follows we describe some methods to improve this low efficiency.

An array of photoconductive antennas will radiate in free-space more THz power than a single antenna and, depending on the type of optical excitation, we can steer the THz beam or control its spectral content (for a review see Ref. [28]). Such an array, the configuration of which is presented in Fig. 8, consists of a sequence of dipole antennas, each of them being independently biased. The THz far-field pattern of the array in the direction θ is given by

$$E_{\text{THz}}(\theta) = \text{const} \times \sum_{n=1}^N [(V_n - V_{n-1})/d] I_n(\Omega) \exp(-inkd \sin \theta), \quad (11)$$

where V_n is the bias applied on the n th electrode, the total number of electrodes (dipoles) being N . $I_n(\Omega)$ is the optical excitation, k is the THz free-space wavenumber and d the spacing between two consecutive photoconductive antennas. If an optical pulse train with period between ultrashort pulses inversely proportional to the emitted THz frequency illuminates the photoconductive array, the direction of the radiation pattern can be scanned about 45° by changing the dc voltage applied to each antenna. If the period of the bias voltage is periodically varied, the array is analogous to a grating that changes the beam direction to a prescribed value given by the bias period. If the bias has a sinusoidal variation $V_n = (E_0/k_b) \cos(nk_b d)$, where $k_b = 2\pi/\Lambda_b$ with Λ_b the bias spatial period, the radiation pattern is given by

$$E_{\text{THz}}(\theta) = \text{const} \times \cos \theta \sin[Nd(k_b \pm k \sin \theta)/2] / \sin[d(k_b \pm k \sin \theta)/2]. \quad (12)$$

Such an array with 32 antenna elements working at 0.5 THz occupies an area of $2 \times 3 \text{ mm}^2$. Each dipole is 2 mm long, $25 \mu\text{m}$ wide and is separated from the next one by $d = 100 \mu\text{m}$. The entire array has a beamwidth with a FWHM of about 10° .

If the array is illuminated by a single optical pulse, the spectral content of the radiated THz signal can be changed by changing the bias. From (10) it follows that the radiation has a maximum at $k_b = \pm k \sin \theta$. Since $k = 2\pi/\lambda$, where λ is the center wavelength of the THz radiation, we have $\lambda = \pm \Lambda_b \sin \theta$, which shows that the THz wavelength is changed when the bias period is varied. For an array with the same dimensions as those given above it was experimentally demonstrated that the frequency can be tuned in the interval 0.140–1.06 THz by changing the bias period from 3 to 0.4 mm.

Recently, miniaturized photoconductive THz sources and probes (detectors) were realized using metal–semiconductor–metal (MSM) interdigitated structures on SOS [29] or LT-GaAs thin substrates [30]. MSM is playing the role of a photoconductive switch, but the transient current is produced due to the ultrafast carrier drift across the gaps formed by the consecutive metal fingers. A part of the optical pulse is directed to the MSM emitter, while the delayed part (probe) is directed to the MSM detector. Thus, we can detect and characterize the radiation of the THz emitter propagated in free-space or in a transmission line due to probe sampling. The photoconductive MSM probe can be used (i) to measure the propagation characteristics of transmission lines at THz frequency emitted by another photoconductive MSM emitter, (ii) to characterize the field distribution of a THz antenna or other THz devices. The THz miniaturized MSM emitter and detector are represented in Fig. 9. The widths of the MSM fingers, as well as the spacing between them, can have a few microns or can even have sub-micron dimensions.

More sophisticated photoconductive antennas can be designed for near-field THz microscopy [31]. For example, a photoconductive antenna realized on a very thin LT-GaAs substrate glued on a thicker sapphire substrate and terminated with a GaAs taper is represented in Fig. 10. The sapphire substrate as well as the taper is designed to reduce the reflections. The THz radiation propagates through a small metallic aperture, a spatial resolution of 60 μm being achieved for a 50 μm aperture.

The latest trends regarding THz photoconductive devices are the integration of the emitter and the receiver on the same chip. The entire device is then called a

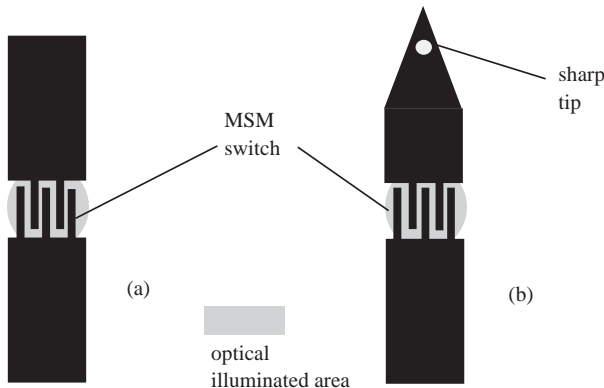


Fig. 9. (a) THz MSM emitter and (b) THz MSM probe (detector).

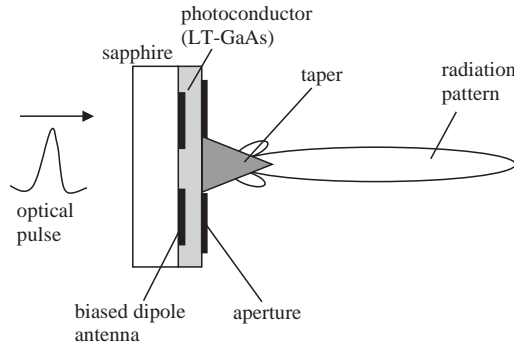


Fig. 10. THz emitter for near field microscopy.

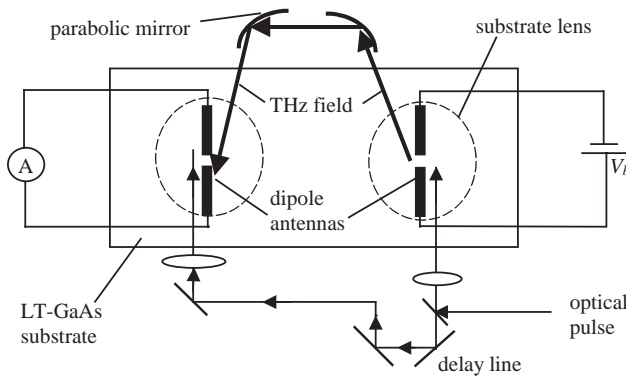


Fig. 11. A photoconductive THz transceiver.

photoconductive transceiver. Since such a single chip device is practically a miniaturized FIR spectrometer, it plays the role of a lab-on-a chip for gas detection or air monitoring. In Fig. 11 we have displayed such a recently reported transceiver using dipole antennas [32]. The distance between the two antennas was 500 μm , each antenna being 10 μm wide and having a gap of 5 μm between each arm of the antenna connected to a feed line that is 100 μm long. The photoconductive LT-GaAs substrate, which had a thickness of 2 μm , was grown on semi-insulating GaAs and the substrate lens had a diameter of 26 mm.

The THz generation method using a CPW line excited by an ultrashort optical pulse (pump) is displayed in Fig. 12. THz detection is realized with the help of a delayed version of the pump (the probe), which shortens the line at a prescribed location. During the photoexcitation produced by the pump the charges are transferred from the CPW central conductor to its ground generating a current flow. Charges of opposite signs accumulated on the two conductors produce a TEM dipolar field. The output voltage is given by

$$v_{\text{out}}(t) = V_b Z_0 g(t). \quad (13)$$

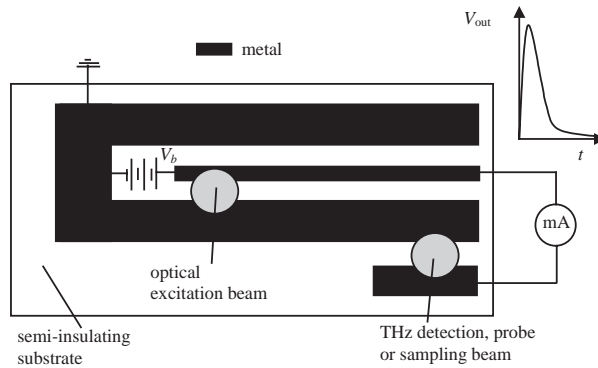


Fig. 12. THz generation using CPW lines.

where $g(t)$ is the photoconductance at the pump location, Z_0 is the characteristic impedance of the CPW and V_b is the bias voltage. Typical values of these parameters are $V_b = 1.5$ V, and $Z_0 = 100 \Omega$; the CPW length is about 20 mm. For a review of THz generation using optically excited CPW see Ref. [33]. The output voltage shows a capacitor-like behavior. The leading edge of the current has a risetime similar to that of the optical pulse, while its trailing edge has a decay time proportional to the carrier's lifetime. An electrical pulse with a symmetrical shape can be obtained if two laser pulses are focused simultaneously between the central and ground electrode of the CPW. Electrical pulses with very short durations (0.4–0.5 ps) can be obtained using this method. A biased CPS line consisting of two electrodes was also used to generate ultrashort electrical pulses using a SOS substrate. By illuminating the positively biased electrode with an ultrashort optical pulse, the transient current produced due to the photoconductive effect can have only 380 fs duration [34]. However, the CPW line is more suitable for THz generation because it can be readily integrated with other THz components. A recent review of THz production using transmission lines can be found in Ref. [35].

High power ultrashort pulses with a spectrum within the THz bandwidth can be generated using large aperture photoconductive antennas. The aperture, which is in fact the gap between the two biased electrodes, as depicted in Fig. 13, allows an illumination area with typical dimensions of a few mm, much greater than the radiated center wavelength. The increased size of the aperture allows the utilization of high optical energies and high values of the bias, high power of the radiated THz field being thus expected. When the energy of the ultrashort optical pulse exceeds the bandgap of the photoconductor, the THz field is generated due to accelerated photocarriers, which produce a transient current at the surface of the biased photoconductor. However, the THz power saturates at high excitation powers due to charge screening effects. The photogenerated electrons and holes move in opposite directions creating spatial regions of positive and negative charges that induce an electrical field in a direction opposite to the applied electric field; for sufficiently large densities of photocarriers the applied electric field can be totally screened [37].

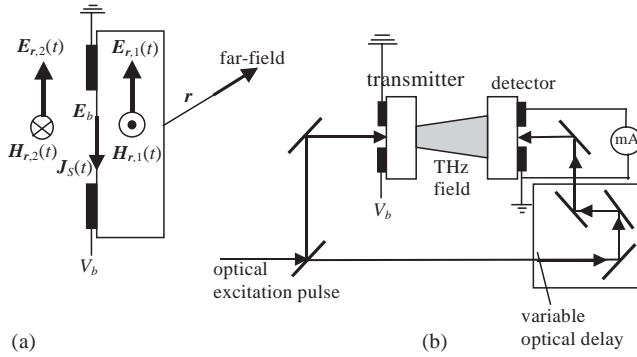


Fig. 13. (a) Distribution of electric and magnetic fields for a large aperture photoconductive antenna, and (b) generation/detection of THz fields using large aperture photoconductive antennas.

Denoting by $E_{r,1}(t)$ and $H_{r,1}(t)$ the electric and magnetic fields, respectively, inside the photoconductor and by $E_{r,2}(t)$ and $H_{r,2}(t)$ the electric and the magnetic fields near the photoconductor surface (near-fields), respectively (see Fig. 13a), the boundary conditions [38] imply that

$$E_{r,1}(t) = E_{r,2}(t) = E_r(t), \quad (14a)$$

$$H_{r,2}(t) - H_{r,1}(t) = J_s(t), \quad (14b)$$

where $H_{r,1}(t) = E_{r,1}(t)\varepsilon^{1/2}/\eta_0$ and $H_{r,2}(t) = E_{r,2}(t)/\eta_0$ with $\eta_0 = 377 \Omega$ the impedance of the free space. With these boundary conditions the radiated electric field is

$$E_r(t) = \eta_0 J_s(t)/(1 + \varepsilon^{1/2}). \quad (15)$$

Taking into account that the Ohm law can be written as $J_s(t) = \sigma(t)[E_b + E_r(t)]$, where $\sigma(t)$ is the surface conductivity, we get

$$J_s(t) = \sigma(t)E_b/[1 + \sigma(t)\eta_0/(1 + \varepsilon^{1/2})]. \quad (16)$$

When $\sigma(t)\eta_0/(1 + \varepsilon^{1/2}) \gg 1$, i.e. at high optical fluence (time-integrated optical intensity), the radiated current saturates and the far-field is given in these conditions by

$$E_r^{\text{THz}} = A[dJ_s(t)/dt]/(4\pi\varepsilon_0 c^2 r). \quad (17)$$

We can see that the near-field is proportional to the surface current, while the far field is proportional to its derivative. Thus, the saturation effect is a near-field phenomenon.

Experiments with large aperture photoconductive antennas have demonstrated high power radiated fields. For example, an electric far field with a value of 0.9 kV/cm and a duration of 1.3 ps was obtained when a InP (1 1 1) substrate was used; when a GaAs (1 1 1) substrate was used the strength of the electric far field reached 1 kV/cm and had a duration of 1.8 ps. In both cases the gap had a value of 0.5 cm, $E_b = 8$ kV/cm and the optical fluence was 1 mJ/cm² [36]. High power and

narrow band THz radiation overcoming the saturation limitations described above can be obtained if the excitation and the thickness of the photoconductive substrate are optimized [38]. Ideally, a multi-pulse excitation should be employed, obtained by splitting the original excitation pulse into N pulses with an interpulse spacing T_s . The multi-pulse excitation is equivalent with single-pulse excitations at the frequencies $\omega = 2\pi m/T_s$, $m = 1, 2, \dots, N$, and produces a THz spectral narrowing when the number of pulses is increased. When the emitter is completely saturated the THz peak power is enhanced by a factor of N^2 . T_s must be 2–3 times larger than the carrier lifetime. THz radiation saturation can also be overcome if the thickness of the photoconductive substrate (LT-GaAs) is chosen such that the light is entirely absorbed into it and not in the substrate on which LT-GaAs is grown. For example, a thickness of at least $3 \mu\text{m}$ is necessary for the photoconducting substrate at an optical excitation at 800 nm.

All types of photoconductive devices used for THz generation presented above are strongly dependent on the properties of the photoconductive substrate and especially on the carrier lifetime. On the contrary, the behavior of the photoconductive switch presented in Fig. 14 does not depend on the properties of the photoconductive substrate. This is possible if the thickness of the photoconductor substrate is smaller than the penetration depth of the optical excitation and if the bottom of the photoconductor substrate is metallized, playing the role of an optical mirror as well as that of an electrical ground plane. For example, at 800 nm the penetration depth in Si is $10 \mu\text{m}$. If we choose this value as the thickness t of the substrate, the optical excitation reaches the ground plane after $\tau_d = tn/c = 110 \text{ fs}$, a time that is shorter than the lifetime of the carriers. In this case the carriers have no time to recombine [39]. The micromachining technology allows the fabrication of Si or GaAs substrates with a thickness less than $2 \mu\text{m}$ [40] so that this photoconductor switch becomes feasible. For a detailed simulation of this device, including a THz equivalent circuit demonstrating the generation of electrical pulses with durations varying from hundreds of fs up to a few ps see Ref. [39].

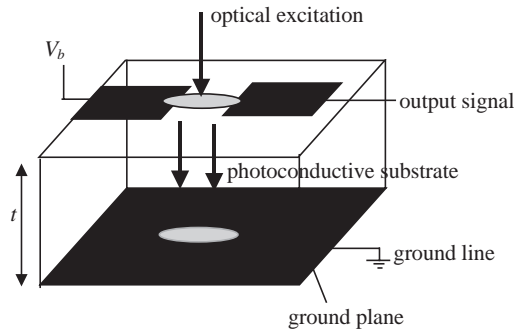


Fig. 14. Photoconductive switch that is independent of the lifetime of the carriers in the photoconductive substrate.

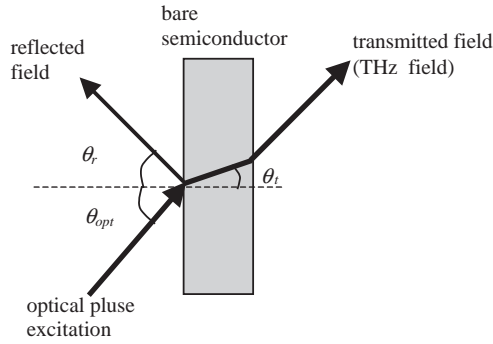


Fig. 15. THz generation using bare semiconductors.

2.1.2. Broadband THz generation from semiconductor surfaces

THz generation from bare semiconductor surfaces is based on the fact that the surface states of many semiconductors surfaces are entirely occupied. As a result the Fermi level is pinned and the conduction and valence bands are bent near the semiconductor surface/air interface creating a depletion region and a strong built-in surface electric field E_b , with a typical value of 10^5 V/cm, perpendicular to the semiconductor/air interface. When an incident ultrashort optical pulse with photon energy greater than the bandgap of the semiconductor hits the semiconductor surface, the injected photocarriers at the semiconductor surface are depleted and accelerated by the built-in field. As a result an ultrashort transient current is formed, which radiates an electromagnetic beam with a spectrum in THz domain (see Fig. 15). Moreover, this beam can be steered by changing the incidence angle of the optical excitation. Many semiconductors such as InP, GaAs, GaSb, InSb, CdTe, CdSe, Ge, and $\text{Ga}_{1-x}\text{Al}_x\text{As}$ ($x < 0.2$) have been used to demonstrate the generation of THz radiation [41]. Also Au/GaAs Schottky barriers can be employed to generate THz radiation at their surface/air interface [42].

The THz field is given by

$$E_{\text{THz}}(t) = Z_s J_s(t) \sin \theta_r / (\cos \theta_r + n \cos \theta_t) \\ = e Z_s [\sin \theta_r / (\cos \theta_r + n_s \cos \theta_t)] \int_0^\infty n(x, t) v(E_b(x, t)) dx \quad (18)$$

where Z_s is the characteristic impedance of the semiconductor, n_s its index of refraction, $n(x, t)$ is the photocarrier density, and $v(E_b(x, t))$ is their drift velocity.

The electric field that accelerates the photocarriers can be generated by the piezoelectric effect in strained superlattices. In this respect, a misfit (111) oriented GaSb/AlSb superlattice has been used to generate THz fields [43]. In comparison to the previous method, the THz signals are generated without an applied bias and an antenna.

In another optical method THz radiation originates from ballistic photocurrents generated due to quantum interference of one and two photons in semi-insulating GaAs and LT-GaAs. THz single-cycle with controllable phase is obtained at the

central frequency of 4 THz with a 3 THz spectral width [44]. In contrast with previous methods, the unbiased photoconductor is excited with two copolarized ultrashort optical pulses having the carrier frequencies ω and 2ω , with $2\hbar\omega > E_g > \hbar\omega$, that couple the same valence and conduction band states through two-photon absorption processes. If the two beams are phase related, the interference between transition amplitudes produces a phase-controllable photocurrent. So, the THz center frequency and bandwidth can be tuned by the optical pulse width, while the THz power is changed by tuning the phases of the two optical pulses. However, the emitted power does not exceed 3.5 nW at room temperature.

2.1.3. Broadband THz generation using optical rectification

Optical rectification is a process inverse to the electro-optic effect, and consists in the generation of an electrical waveform that is the envelope of an ultrafast optical pulse, which excites an electro-optical material. Materials suitable for this method include among others LiNbO_3 , LaTiO_3 , zinc-blende semiconductors (GaAs, ZnTe, CdTe, InP) or organic crystals (DAST). The physical mechanism involved in optical rectification is the production of a transient polarization $P(t)$, when a fs optical pulse is focused on an electro-optical material. The THz radiation is proportional to the second time derivative of the low-frequency part of $P(t)$ analogous to the case of a transient dipole. Detailed reviews of this method can be found in Refs. [45,46].

Very short electrical pulses are obtained with this method, much shorter than in the case of the photoconductive method. For example, in Ref. [47] a bipolar pulse with a FWHM of 180 fs is produced using optical rectification. The efficiency of this method depends on the optical second-order nonlinear coefficients ($\chi^{(2)}$) of the materials, and on the phase matching conditions. The power of the THz radiation produced by this method is lower than that produced using the photoconductive method, but its spectral content is much broader attaining 50 THz [48].

Zinc-blende semiconductors are among the most commonly used materials for THz generation/detection by optical rectification. When the photon energy is greater than the semiconductor bandgap ($E_{\text{photon}} > E_g$), as in the case of unbiased GaAs, THz generation originates from two mechanisms: the carrier's acceleration, as described in the previous paragraph, and optical rectification. The first mechanism is cancelled by illuminating the sample at normal incidence, so that only optical rectification is contributing [49]. Also, optical rectification can be obtained by illuminating the semiconductor with photons that have a smaller energy than the semiconductor bandgap ($E_{\text{photon}} < E_g$). The value of the generated signal depends strongly on the orientation of the optical polarization and on the crystallographic orientation of the sample. A THz system using optical rectification is presented in Fig. 16. The detection technique is based on electro-optic sampling, which will be described in Section 4.1. It is important to mention that the two ZnTe crystals at the emission and detection are identical, and are separated by a few tens of centimeters, which is the free space distance of THz fields propagation.

The key problem in optical rectification is the phase matching, which maximizes the interaction between the optical and the THz pulse in the nonlinear material and thus enhances the efficiency of THz generation. The optical rectification process, in

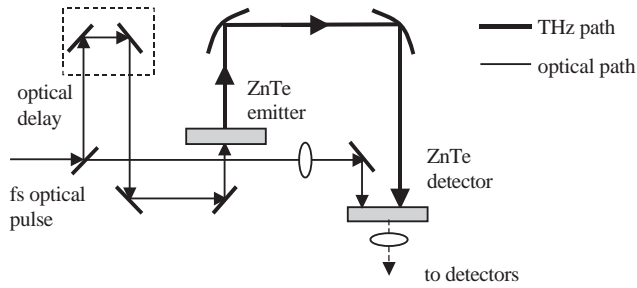


Fig. 16. THz generation using optical rectification.

which a THz pulse with frequency ω_{THz} collinear with the optical pulse is produced, can be viewed as mixing of different spectral components ω_{opt} and $\omega_{\text{opt}} + \omega_{\text{THz}}$ of the optical pulse [50]. The phase matching condition for the wavenumbers at different frequencies is

$$\Delta k = k(\omega_{\text{opt}} + \omega_{\text{THz}}) - k(\omega_{\text{opt}}) - k(\omega_{\text{THz}}) = 0. \quad (19)$$

Neglecting optical dispersion, the coherence length is

$$l_c = \pi / \Delta k = \pi c / (\omega_{\text{THz}} |n_{\text{opt}} - n_{\text{THz}}|), \quad (20)$$

where n_{opt} and n_{THz} are the refractive indices at the optical and THz frequencies, respectively. Long coherence lengths can be obtained using either birefringence or angle tuning in noncollinear configurations. The dispersion of the optical refractive index is also a way to increase the coherence length in a large THz bandwidth [50]. In this case, the phase matching is obtained when the THz pulse propagates with the group velocity of the optical envelope. In this case, the coherence length is given by

$$l_c = \frac{\pi c}{\omega_{\text{THz}} |n_{\text{opt}} - \lambda_{\text{opt}} (dn_{\text{opt}}/d\lambda)|_{\lambda_{\text{opt}}} - n_{\text{THz}}|}. \quad (21)$$

In the case of ZnTe at $\lambda_{\text{opt}} = 800$ nm the coherence length is large in the bandwidth 0.5–2 THz. A simple and efficient phase matching technique demonstrated theoretically and experimentally in the GHz–THz range is based on a rectangular waveguide partially filled with a nonlinear crystal. Controlling the filling degree of the rectangular waveguide very efficient collinear phase matching and thus more efficient THz generation can be obtained [51].

2.1.4. Broadband THz generation using nonlinear transmission lines

Nonlinear transmission lines (NLTL) are distributed devices, which consist of a high impedance transmission line, usually a CPW line, periodically loaded with nonlinear elements, usually Schottky varactor diodes. The concept of a NLTL device is presented in Fig. 17, where the nonlinear elements are diodes with a nonlinear capacitance $C(V)$, with V the voltage applied on them. The entire device can be monolithically integrated using the GaAs technology, which is necessary to build Schottky diodes with a cutoff frequency beyond 1 THz. Shock waves or solitons can occur in NLTL devices due to the balance between the nonlinearity and inherent

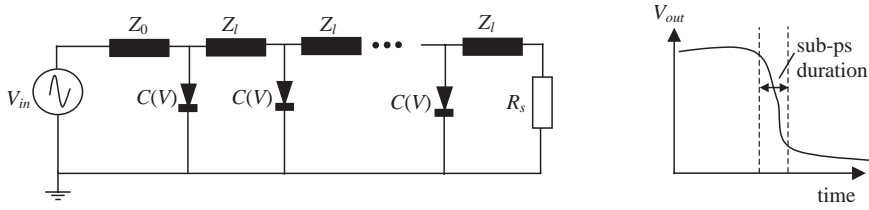


Fig. 17. A NLTL device.

dispersion. Both waves are compressed versions of the input excitation, which is a high power microwave sinusoidal wave. We consider that the CPW line impedance Z_l is formed by a series inductance L_l and a shunt capacitance C_l and that the Schottky diode can be modeled with a resistance (R_d) in series with a variable capacitor (C_d). The NLTL behavior can be characterized with the help of two frequencies:

$$f_d = [2\pi R_d C_d(V)]^{-1}, \quad (22)$$

$$f_b = \frac{1}{\pi L_l [C_l + C_d(V)]^{1/2}}, \quad (23)$$

where f_d is the cutoff frequency of the diode and f_b is the cutoff frequency of the NLTL circuit. Shock waves with a shape similar to that shown in Fig. 17 are generated if $f_d = f_b$ and soliton waves are formed if $f_d \gg f_b$. The soliton wave is produced due to the balance between dispersion and nonlinearity of the propagating wave in the NLTL. The solitons are described by a Korteweg de Vries (KdV)-like nonlinear equation and have a sech^2 shape.

In the case of shock wave generation, the delay between two consecutive cells is $\tau = d/v_{\text{CPW}}$, where d is distance between two consecutive diodes and $v_{\text{CPW}} = 1.13 \times 10^8$ m/s (for GaAs) is the propagation velocity in the CPW, $L_l = \tau Z_l$ and $C_l = \tau/Z_l$. The shock wave effect can be described as follows: the negative part of the input sinusoidal voltage propagates along the NLTL, its fall time decreasing as a function of distance. After propagating through n -cells, the fall time is

$$t_n = t_{\text{in}} - n\tau \{ [1 + C_d(0)/C_l]^{1/2} - [1 + C_d(-V_{\text{MAX}})/C_l]^{1/2} \}. \quad (24)$$

When the fall time decreases, the dispersion that broadens the fall time is balanced by the nonlinearity, which compresses the fall time due the voltage-dependent propagation velocity. A stable fall time of the input voltage (the shock wave) is attained when the fall time compression/cell is equal to the fall time broadening/cell. After this, the shock wave propagates unchanged in shape along the NLTL.

A step-like shock wave of 3.5 V amplitude and 480 fs 10–90% fall time was obtained using delta-doped Schottky varactors; its spectral content was found to exceed 3 THz [52]. Moreover, an all-electronic THz spectroscopic system based on NLTL was implemented for the amplitude and phase measurements of various samples in the range 0.2–1 THz [53]. Extensive reviews about nonlinear waves and NLTL devices for millimeter and submillimeter waves can be found in Refs. [54,55].

Recently it was analytically and numerically shown that solitons with a duration of 2.7 ps can propagate in a NLTL consisting of $n = 60$ quantum barrier varactors, named also heterostructure barrier varactors (HBV) [56]. The dependence of HBV capacitance with the applied voltage can be expressed as

$$C(V) = C(0) + C_{\max} \operatorname{sech}(\Delta_c V), \quad (25)$$

where $C(0)$ is the unbiased value of the HBV capacitance, C_{\max} is the maximum value of the HBV capacitance and Δ_c is the width of the $C(V)$ curve.

2.2. Narrowband THz generation

This section is dedicated to the generation of CW THz fields. In contrast with the THz sources presented in Section 2.1, the THz sources presented below are characterized by a spectrum consisting of a single spike centered within the THz range with a very narrow bandwidth. A very large tunability of this CW component inside the THz bandwidth and a power as large as possible are highly desirable. As in the last section, these aims will be fulfilled using methods that combine optical and electronic means (THz photomixing), only optical means (THz parametric generation), or solid state devices such as resonant tunneling diodes, multipliers and solid state lasers. The THz CW signals are of considerable importance for high-resolution THz spectroscopy, THz sensors and ultrabroadband communications.

Traditionally, gas lasers generate CW THz signals in the frequency domain 0.9–3 THz with output powers in the range of 1–30 mW. A gas laser consists of a carbon dioxide laser that pumps a cavity filled with a gas such as CH_4 , N_2 , etc., which dictates the lasing frequency. The gas sources show no tunability and are very large, with dimensions exceeding 2.5 m. However, a “miniaturized” version of a gas laser was recently reported, which delivers 30 mW at 2.5 THz, its dimensions are $75 \times 30 \times 10$ cm and weight 20 kg [57].

Free-electron lasers generate either CW or pulsed high power THz radiation, but they are very costly and have very large dimensions, functioning in large rooms containing many additional facilities. Therefore, only a few are operating in the world. However, backward wave oscillators (BWO) are based on the same principles as an electron laser and are able to deliver a few mW in the range of 0.6–1.3 THz. In contrast with THz gas lasers, BWO are frequency tunable (for example, between 0.78 and 0.97 THz or 1 and 1.25 THz) with a high sweeping rate. BWO requires a water-cooling system and high bias voltages of 1–6 kV at 25–45 mA. The weight of a BWO (without the cooling system and the power supplies) is more than 15 kg.

However, THz gas lasers and BWOs are commercially available, being the only CW THz sources that can be bought from the market. They are both bulky and need a lot of accessories such as high power supplies, water-cooling systems, etc.

It is now understandable why so many efforts were dedicated in the last decade in the quest of a miniaturized CW THz source working at room temperature and delivering a few mW output power. As we will see, this quest continues, because the performances mentioned above were only partially achieved up to now.

2.2.1. Narrowband THz generation based on photomixing

Heterodyne mixing (photomixing) of two individual optical CW lasers (one of them being tunable) in a photoconductor produces a photocurrent with a frequency equal to the difference between the frequencies of the two lasers. When this difference frequency is within the THz range of frequencies the photocurrent is propagated along the transmission line or is radiated in free-space with the help of an antenna. There are two types of photomixers: discrete-element photomixers and distributed photomixers. Discrete-element photomixers are photoconductors, such as micrometric photoconductive gaps or MSM interdigitated structures, with a large bias field applied between their electrodes, illuminated by the two lasers sources and placed at the driving point of an antenna or an antenna array. Discrete-element photomixers act like a current source with a very wide bandwidth and drive the antenna at THz frequencies. The distributed photomixers are based on similar principles, except that the optical field produced by the lasers propagates along the photomixer structure and is not localized in a single point, as in the case of discrete-element photomixers. Recent comprehensive reviews about photomixers are found in Refs. [58,59].

Different configurations of discrete-element photomixers, which will be analyzed in what follows, are represented in Fig. 18. Since there are a lot of photoconductor and antenna geometries, many combinations between them can be imagined; only a few of them are represented in Fig. 18. Basically, the photomixer can be modeled as a photoconductor with a photoconductance $G(t)$ variable in time. This photoconductance is in parallel with the capacitance C , which depends on the photoconductor geometry (gap, interdigitated, etc.). The equivalent circuit model of the photomixer is represented in Fig. 19, where $Z_A = R_A + iX_A$ is the antenna radiation impedance.

We consider that the incident optical power, which illuminates the photomixer, is given by

$$P_i(t) = P_1 + P_2 + (P_1 P_2)^{1/2} \{ \cos[2\pi(f_2 - f_1)t] + \cos[2\pi(f_2 + f_1)t] \}, \quad (26)$$

where P_1 and P_2 are the optical powers, and f_1 and f_2 the frequencies generated by the first and the second laser, respectively. The photon energies of the two lasers hf_1 and hf_2 must be greater than the bandgap energy of the LT-GaAs photoconductor (1.4 eV). The frequency which modulates the photoconductance is $|f_1 - f_2| = f_{\text{THz}}$ since the term in Eq. (26) containing the sum of frequencies varies on a much shorter time scale than the lifetime of the photoconductor, τ . The time variation of the photoconductance is given by [60]

$$G(t) = G_0 \{ 1 + \beta \sin(\omega_{\text{THz}} t) [1 + (\omega_{\text{THz}} \tau)^2]^{-1/2} \}, \quad (27)$$

where G_0 and β are dependent on the input optical power $P_0 = P_1 + P_2$ and the geometry of the electrodes that form the photoconductor. The voltage dropping on the photoconductance, v , is described with the help of the equivalent circuit and is given by the equation

$$C dv/dt = (V_b - v)/Z - G(t)v. \quad (28)$$

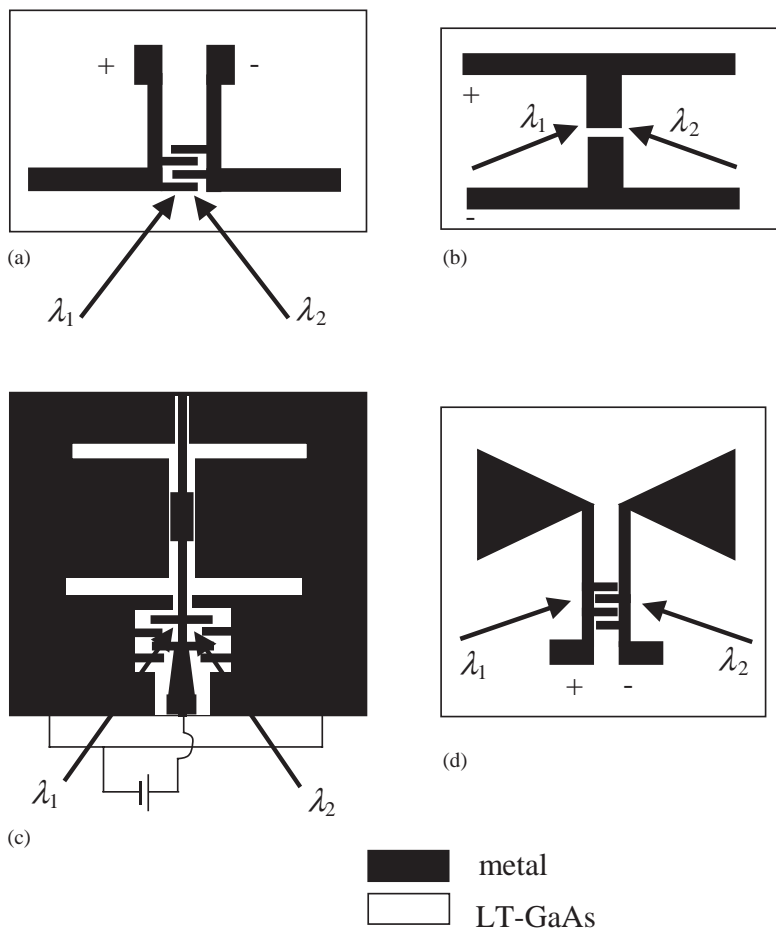


Fig. 18. Discrete-element photomixer geometries: (a) MSM photoconductor with dipole antenna, (b) gap photoconductor with dipole antenna, (c) MSM photoconductor with CPW double slot antenna, and (d) MSM photoconductor with bowtie antenna.

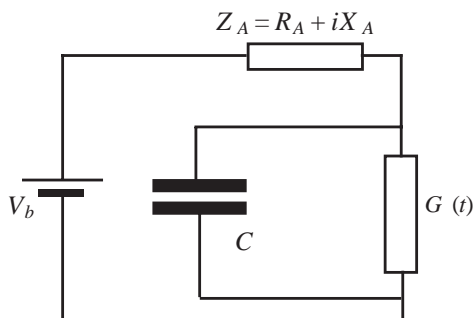


Fig. 19. Equivalent circuit of a discrete-element photomixer.

Solving this equation with the assumptions that v has a sinusoidal variation, that $P_1 = P_2 = P_0/2$ and that the antenna impedance is resistive, i.e. $Z_A = R_A$, we obtain the power radiated at THz frequencies as

$$P_{\text{THz}} = \frac{(G_0 V_b)^2 R_A}{2[1 + (\omega_{\text{THz}} \tau)^2][1 + (\omega_{\text{THz}} R_A C)^2]} \quad (29)$$

The formula above provides guidance for increasing the output power of THz photomixers as much as possible. According to it, in the limit of ultrahigh frequencies, where $\omega \tau \gg 1$ and $\omega R_A C \gg 1$, the photomixer that acts as a current source, i.e. for which $G_0 R_A \ll 1$, must have a low capacitance C and a very low value of the carrier lifetime τ . To this end photoconductor electrodes with a small area must be used. For example, in the case of MSM interdigitated electrodes an area of $8 \times 8 \mu\text{m}$ with a $1.8 \mu\text{m}$ gap between two consecutive fingers was used, the fingers having a width of only $0.2 \mu\text{m}$. A typical value for C , valid for any type of electrode geometry, is $0.5\text{--}1.5 \text{ fF}$, while $G_0 = 2 \times 10^{-5} \text{ mho}$. Eq. (29) suggests also that an antenna with a high R_A will produce high THz output powers. Therefore, there are many photomixers based on dipoles, dual dipoles or dual-slot antennas, as well as bowtie antennas, which show radiation resistances of about 300Ω when properly biased and working near resonance [61–64].

The THz output power can be written also as

$$P_{\text{THz}} = \frac{R_A \eta^2 \lambda_1 \lambda_2 (e/hc)^2 P_1 P_2}{2[1 + (\omega_{\text{THz}} \tau)^2][1 + (1 + \omega_{\text{THz}} R_A C)^2]} \quad (30)$$

where η is the external quantum efficiency. This expression apparently indicates that a higher THz power could be obtained if the power of the optical sources is increased. However, it was observed that beyond a certain optical power (tens of mW) the photomixer is destroyed due to thermal failures [65]. Despite all the efforts the THz power obtained using photomixers is still very low: about $1 \mu\text{W}$ at 1 THz and $0.2 \mu\text{W}$ at 2 THz .

The reason is that the external quantum efficiency is very low, which means that the optical heterodyne process has a very poor efficiency. The external efficiency can be written as $\eta = gA$ where g is the number of electrons induced in the antenna per absorbed photon (photoconductive gain) and A is the fraction of incident power absorbed in the photoconductive substrate. Extensive numerical calculations have shown that the optical intensity inside the photomixer is smaller than one-half of the incident intensity and the majority of the photocarriers are generated deep in the photoconductor, where g is low [66]. In this situation, the external efficiency is about 0.008. An increase of η can be achieved if the thickness of the LT-GaAs layer is smaller than $1/\alpha$, where α is the absorption coefficient at the optical field wavelength, and is backed by a mirror. An optimal photomixer structure consists then from a $0.35\text{--}0.5 \mu\text{m}$ thick LT-GaAs layer, followed by a buried $2.5 \mu\text{m}$ thick AlAs layer, which enhances thermal dissipation since the thermal conductivity of AlAs is two times larger than that of LT-GaAs, and ends with a DBR AlAs/ $\text{Al}_{0.05}\text{Ga}_{0.95}\text{As}$ mirror having 2–3 periods. All these substrates form an optical cavity between the top of the mirror and the top of the LT-GaAs. Even employing this optimal

structure, in which η is increased 3 times and thus the output power is enhanced by a factor of 9, the THz power does not exceed a few μW .

Lowering the carrier lifetime could be another way to increase the output power of a photomixer. In this respect, self-assembled ErAs islands in GaAs were used to build a heterostructure consisting of alternative layers of GaAs and ErAs islands [67]. Although the carrier lifetime was reduced to 0.1 fs, i.e. 2.5 times lower than in the LT-GaAs, the output power was still only 0.1 μW at 1 THz before the thermal failure of the device.

New concepts of photomixers are developing using, for example, asymmetric p–i–n–p–i–n heterostructures consisting of consecutive δ -doped n and p GaAs layers and incorporating ultrathin LT-GaAs or ErAs layers between the n and p layers [68]. In this device the carriers move ballistically due to the very high electric field (of about 20 kV/cm) applied on the structure, which produces a sharp peak of the drift velocities (10^8 cm/s) in a short time interval of a few hundreds fs after which the drift velocity takes its static value of about 10^7 cm/s. If the transit time through the device has a similar duration the ballistic transport is assured and thus the thorny problem of the carrier lifetime is eliminated. To reduce the transit time the length of this device should be of only 200 nm but, assuming a cross-section of $5 \times 5 \mu\text{m}^2$, the device is expected to deliver 0.1 mW at 1 THz for an optical power of 10 mW.

A vertically integrated photomixer was realized recently [69]. A thin layer of LT-GaAs with a thickness of 1.8 μm is sandwiched between two metal plates. These metal plates are connected via a semitransparent pad and a buried contact to the two metallic arms of an antenna, which have a spiral shape and are located at top and bottom surface of the photomixer, respectively. This MSM-like photomixer requires for its implementation only 1 μm scale standard photolithography techniques, while the interdigitated MSM photomixers described above, with fingers with submicron dimensions, can be realized using only electron-beam lithography. The MSM-like photomixer has demonstrated an output power of 0.5 μW at 1 THz and a responsivity of 0.04 A/W at a bias of 8V.

Discrete-element photomixers have small active areas not exceeding $10 \times 10 \mu\text{m}^2$, carriers with low lifetimes and electrodes with small capacitances and sub-micron electrode gaps, which provide high photocurrents. These characteristics lower the output power. In contrast, traveling-wave photomixers use much larger active areas, of the order of $10^3 \mu\text{m}^2$ (see Fig. 20a and b). When the second laser beam with a frequency f_2 is superimposed on the same spot as the first laser beam, which has a frequency $f_1 > f_2$, an interference fringe pattern oscillating at $f = f_1 - f_2$ is produced. The spatial distribution of the photocarriers has the same shape as the interference pattern and the output power reaches a maximum value when the velocity of the optical interference fringes (v_{opt}) equals the group velocity (v_{THz}) of the THz signal (the photocurrent) [70]. In the case of the photomixer displayed in Fig. 20

$$v_{\text{opt}} = c(f_1 - f_2)/(f_1 \sin \theta_1 - f_2 \sin \theta_2), \quad (31)$$

and

$$v_{\text{THz}} = c/[(1 + \epsilon_r)/2]^{1/2}. \quad (32)$$

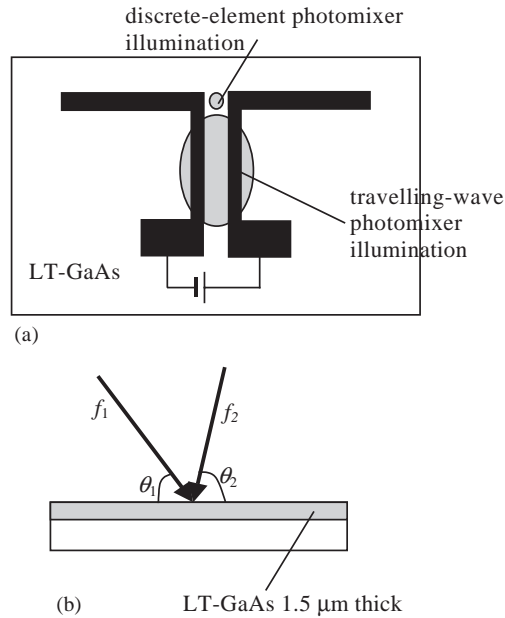


Fig. 20. Traveling-wave photomixer: (a) the basic concept, and (b) the position of the two lasers.

It is obvious that the equality between the two speeds can be easily accomplished by tuning the angle of incidence of one laser. This type of photomixer produces powers larger than 10 μ W.

The above photomixer was realized on a thick substrate, the LT-GaAs being grown on a semi-insulating GaAs substrate, and thus a lot of power was lost in the dielectric substrate due to unwanted radiation. An optimized version of this traveling-wave photomixer, put forward recently in Ref. [71], employs a CPW line (instead of a CPS) and is terminated with a double slot antenna (in the place of the dipole), both supported on a very thin micromachined LT-GaAs membrane of 1.5 μ m and separated by an air substrate from a metallic area acting as reflector and ground plane.

A last but very important problem of photomixers is the synthesis of the difference of the optical frequencies. This is done with two CW semiconductor lasers, which are phase-locked, one of the lasers being tunable. Practically, most of the references in this paragraph indicate the experimental laser configuration used to synthesize the desired frequencies that excite the photomixer. For example, a very reliable and relatively easy way to implement the scheme able to synthesize precisely the required difference of frequencies is presented in Ref. [70]. An optical difference frequency synthesizer up to 3.17 THz, very stable and with a very good signal-to-noise ratio, based on optical combs, is described in [72]. A review focused on various solutions for optical difference frequency generation can be found in Ref. [73].

The synthesis of optical difference frequencies is generally implemented with quite complicated setups. A simpler solution is the utilization of the light produced by a

commercially available multimode laser diode modulated in intensity by the beat frequency between cavity modes [74]. The best solution is a single optical device—a coupled-cavity vertical emitting semiconductor laser (VCSEL)—in which the optical frequencies f_1 and f_2 are separately generated in each of the coupled cavities and the optical beating is directly produced in the two-mode operation of the VCSEL. An additional advantage is that, in this case, the optical difference frequency is independent of any thermal drift [75].

2.2.2. Narrowband THz generation using optical parametric conversion

Continuous tunable CW THz frequencies can be obtained by parametric light scattering from the stimulated polariton scattering in nonlinear crystals. Optical nonlinear crystals such as LiNbO₃ or MgO doped LiNbO₃ produce stimulated polariton scattering when they are strongly pumped with a ns pulsed laser in the near-infrared region ($\lambda = 1.064 \mu\text{m}$) that has a repetition rate of several Hz and a pulse energy in the range 20–50 mJ/pulse. The pump wave with frequency ω_P generates an idler wave with a different frequency, ω_I , when it excites a cavity formed by the nonlinear crystal positioned between two mirrors. On its turn, the idler wave is beating with the pump wave and thus generates a THz wave according to the law $\omega_P = \omega_I + \omega_{\text{THz}}$ (see Fig. 21). The THz wave is outcoupled from the cavity by a Si prism. This parametric process is possible because polaritons behave like photons in their spectral low-frequency region, including the THz region. In stimulated processes, the momentum is conserved; this requirement imposes the phase-matching condition $\mathbf{k}_P = \mathbf{k}_I + \mathbf{k}_{\text{THz}}$, which indicates that the THz frequency can be tuned changing the angle of incidence, θ_{in} , of the pump.

The envelope of the THz signal generated in the way indicated above is a pulse with a duration of 3–4 ns, so that the THz signal oscillating at a ps scale can be viewed as a CW source with a large range of tunability (0.7–3 THz) and high peak-powers (100 mW). The conversion efficiency is with 3–4 orders of magnitudes greater than that obtained using the photomixing method. However, since the pump is a bulky Q-switch Nd:YAG laser and since the distance between the mirrors of the optical cavity is 15 cm (only the nonlinear crystal is 6.5 cm long) this THz source is not miniaturized, but fits on a tabletop. Extensive reviews of this method of THz generation can be found in Refs. [76,77].

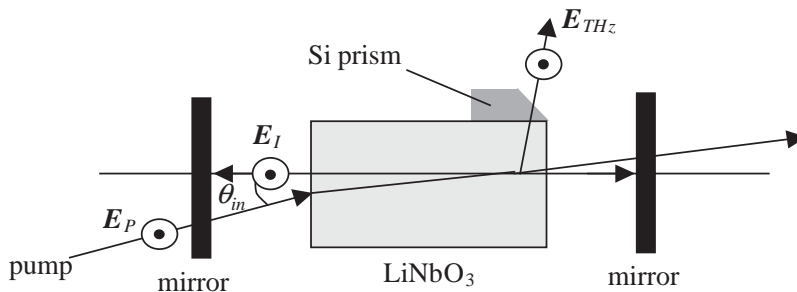


Fig. 21. Optical parametric generation of THz radiation.

2.2.3. Narrowband THz generation using electronic devices

Presently, there is no single electronic device able to oscillate in the bandwidth 1–3 THz. Only resonant tunneling diodes were able to oscillate around 700 GHz, other microwave and millimeterwave active devices, such as Gunn diodes or Impatt diodes, being not able to exceed oscillating frequencies beyond 400–500 GHz. An updated review of these devices can be found in Ref. [78]. InP Gunn oscillators are able to generate 30 mW at 193 GHz, 3 mW at 300 GHz and more than 1 mW at 315 GHz, while a GaAs tunnel injection transit time diode (TUNNETT) produces 10 mW at 202 GHz [79]. Very recently it was theoretically shown that a unipolar TUNNETT heterostructure can oscillate in the THz range when the electrons are injected through tunneling of a square barrier into a very short (50–100 nm) transit space where they are ballistically transported to an anode. The anode is made from a material that allows no reflection and no backscattering of incoming ballistic electrons [80].

Therefore, multiplication circuits are used to generate THz frequencies. A multiplier consists of a nonlinear electronic device, such as a Schottky varactor diode or a HBV diode, placed between an input and an output-matching network. HBV diodes made on a gold substrate are very appealing for multiplication purposes [81]. The gold substrate offers mechanical stability and is in the same time a heat sink for the device. The literature dedicated to millimeterwave multipliers is huge and, due to this reason, these circuits will not be described in detail here. In this respect, the reader is advised to read two extensive reviews: Refs. [82,83].

The output frequency of a multiplication circuit can be designed, using specific rules, to be a multiple of its input frequency (pump): $f_{\text{out}} = mf_{\text{in}}$. Unfortunately, the output power is much lower than that of the pump, which is a serious drawback for the THz frequency range. A pump with a power of 200–300 mW at 100 GHz can be produced by HEMT amplifiers, but a multiplier with a high-order of multiplication from 100 GHz up to 1–3 THz is not feasible due to the very high losses. Much lower losses are achievable only in multipliers with a low-order of multiplication, i.e. doublers ($\times 2$) and triplers ($\times 3$), so that a THz multiplier could consist of a sequence of doublers and triplers of the frequency up to the desired THz frequency.

The main problem encountered in any THz electronic circuit are the dielectric losses in the semiconductor substrate, which supports the diodes and the metallic circuitry necessary for matching or propagating THz waves. The solution is the thinning of the semiconductor substrate up to a thickness of 1–3 μm using MEMS technologies [84]. Only in this way the output power of THz multipliers can be substantially increased. In this respect, planar THz multipliers were realized using two techniques displayed schematically in Figs. 22 and 23. The entire passive network of the planar multipliers was made either on a thin membrane of GaAs (3 μm thickness) supported on a waveguide block or suspended in air by removing entirely the substrate under the metallic circuitry (“substrateless” technique).

Impressive results were achieved using these MEMS techniques utilized in the micromachining of semiconductor substrates. For example, 400 GHz and 800 GHz doublers with a few mW output power and efficiencies of 15–20% were realized using the substrateless technique. The first planar Schottky multiplier working

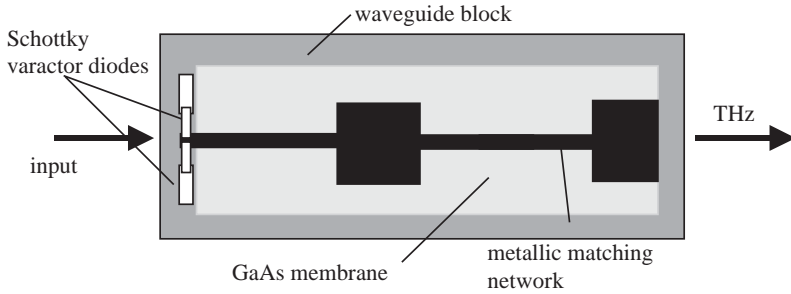


Fig. 22. Part of a THz multiplier illustrating the thin membrane technique used for passive circuitry.

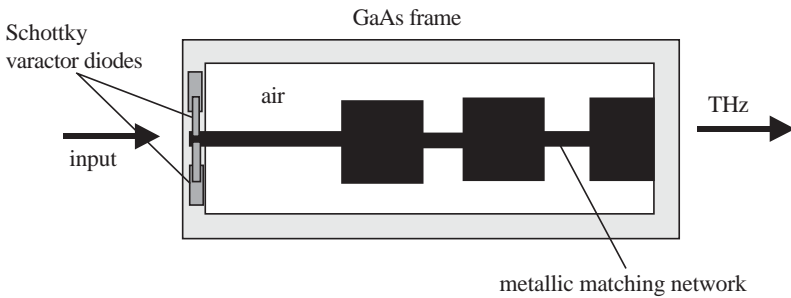


Fig. 23. Part of a THz multiplier illustrating the “substrateless” technique for passive circuitry (suspended in the air).

beyond 1 THz was realized using the membrane technique. At 1.2 THz this device produces 80 μW output power at room temperature, 200 μW at 120 K, and 250 μW at 50 K. A tripler at 2.7 GHz with a 1 μW output power was fabricated using the same technique [85,86]. THz multipliers will play a major role in future THz technology since they are compact and show a high-degree of integrability. Although, the planar THz multipliers using MEMS techniques are 2–3 years old, they already surpass the performances of some optical techniques involved in THz generation.

2.2.4. THz generation using semiconductor lasers, masers, tasers

The subject of this section is a hot topic in the area of THz fields, being boosted by the need of a single miniaturized device working at these frequencies and able to provide a few milliwatt of THz power at room temperature. Although there are an impressive number of proposals for THz semiconductor lasers based on very complicated calculations and simulations, there are very few experimental results regarding their performances. THz lasers can be found in literature under various names such as masers or tasers, all of these devices having in common the inversion of population between two or more discrete energy levels and the generation of THz stimulated emission.

The available experimental results show that, despite many efforts paid in the last two decades to develop a THz semiconductor laser, all the existing THz semiconductor lasers work well only at low temperatures. However, there are some important results obtained in the last years, which show that a THz semiconductor laser working efficiently at room temperature could be realized in the next years.

The first THz semiconductor laser was a single crystal of p-doped Ge placed between two mirrors. The dimensions of the rectangular parallelepiped Ge crystal are about $5 \times 7 \times 50 \text{ mm}^3$ [87]. The THz field is produced due to inversion of the hole population between the LH and HH bands induced by perpendicular electric and magnetic fields, the amplitudes of which are in a ratio of about $|E/H| = 1.5 \text{ kV/cmT}$. The electric and magnetic fields accelerate the heavy holes above the optical phonon energies; part of them are scattered in the LH band where light-holes are accumulated on closed paths just below optical photon energy. The inversion of the population produces THz radiation that can be tuned in the range 1–4 THz by tuning the magnetic field. The p-Ge laser has a low efficiency and is cryogenically cooled at 4–5 K.

The tremendous technological realizations in semiconductor heterostructures, which allow the engineering of semiconductor bands and thus the engineering of the heterostructure properties, have boosted a vigorous quest for the search of THz lasers. The result of this quest is the quantum cascade laser, proposed in 1971 [88] as a FIR radiation source. In a quantum cascade laser the light produced by one carrier transition between two levels is amplified due to photon-assisted tunneling of a single type of carriers in a sequence of coupled quantum wells (superlattice) that has a staircase-like band energy. The number of amplification stages dictates the output power. The practical implementation of this laser was achieved in 1994 (after 23 years!) at Bell Laboratories. This laser is very different compared to usual semiconductor lasers. It is a unipolar laser where the carriers can be either electrons or holes. Only in this way it is possible to use the transitions within the same band, which can be either the conduction or the valence band. The discreteness of energy levels, named subbands, inside the same band is a result of the spatial confinement of carriers inside the heterostructure. The band energy of a cascade laser is presented in Fig. 24.

The FIR radiation frequency is determined by the energy difference of subbands between which radiative/lasing transitions occur. The energies of subbands are, in turn, governed by the thickness of the semiconductor layer that plays the role of well

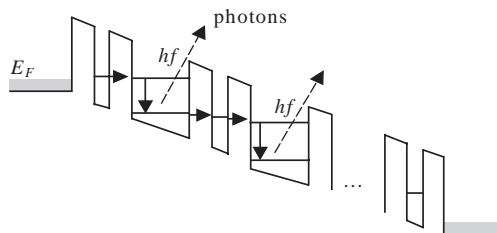


Fig. 24. Quantum cascade tunneling laser.

for the carriers involved in the lasing transition. The radiative transitions can take place between the excited state and the ground state of the same quantum well or between discrete levels in two adjacent quantum wells, case in which the transition is called oblique. In both cases, the applied field must align the lower and upper energy levels of subsequent transitions such that the carriers can tunnel between adjacent wells. Quantum tunneling is the fastest way to transfer carriers from one quantum well to another with a very low scattering rate. In the structure in Fig. 24 the quantum wells in which radiative transitions occur are separated by wells with a single discrete energy level in resonance with the lower and upper energy levels in the adjacent quantum wells; the quantum tunneling at this energy level is resonant. Resonant tunneling is characterized by a transmission close to unity and by the fastest tunneling time.

The inversion of population (in particular, electrons) between the subbands involved in the radiative transition takes place inside every quantum well of the quantum cascade structure, the population of the upper level increasing with respect to that of the lower level due to the fast depletion of the lower level population caused by tunneling of electrons to the upper level of the next quantum well. In this way, like in a cascade, each electron generates (ideally) a number of photons equal to the total number of quantum wells (or subsequent transitions).

Very recent reviews on the state of the art of quantum cascade lasers and their applications can be found in Refs. [89,90]. An in-depth analysis of various types of quantum cascade lasers and their modeling can be found in Ref. [91].

InGaAs/InAlAs/InP and GaAs/AlAs heterostructures were used to generate FIR at room temperature in the wavelength range 17–90 μm . The first quantum cascade laser working in the THz range was reported very recently [4]. The realization of a quantum cascade laser at THz frequencies encounters a series of difficulties and limitations due to the very large values of the wavelength. Among them are very large free-carrier absorption losses and the necessity of growing a very thick heterostructure. The 4.4 THz quantum laser mentioned above had 104 periods, each period containing 7 coupled quantum wells, each quantum well having two AlGaAs barriers (with a thickness of 1–4 nm) and one GaAs well (10–20 nm thick), resulting in a total number of 728 quantum wells (!). It is not at all easy to manufacture such a heterostructure. This laser delivers about 2 mW power at 4.4 THz and is operating at 50 K. The output power decreases dramatically with increasing temperature and becomes nearly zero at room temperature. However, this THz laser is considered a huge step forward towards THz miniaturized sources. A low threshold THz quantum cascade laser was reported in Ref. [92]. It contains a three-quantum-well chirped superlattice active region located inside a waveguide, the total heterostructure being 2.7 mm long. The threshold current of this THz laser is only 210 A/cm²; it operates at 66 μm and delivers 4 mW at 12 K. All these THz cascade lasers are based on n-type carriers (electrons) and the photon emission is parallel to the heterostructure plane (edge-emission).

The operating temperature of quantum cascade lasers can be increased by replacing the InP or GaAs based heterostructure with the one based on Si. A THz quantum cascade laser based on the Si/SiGe material system could attain room

temperature operation due to the absence of strong polar optical phonon scattering. Such a THz laser is also unipolar and its frequency is determined by subband energy spacing, but the carriers are p-type (holes) and the photons are emitted normal to the heterostructure plane. Thus, a THz Si/SiGe laser is a THz VCSEL laser, which is easily integrable with THz waveguides and can be easily arranged in 2D arrays. There are some proposals of THz Si/SiGe lasers based on transitions between LH and HH subbands using the inverted masses concept [93], or phonon pumping [94].

All lasers mentioned above are electrically pumped (the carriers are injected from carrier reservoirs—leads—by applying a bias) but there are THz lasers, which are optically pumped, the lasing being based on intersubband emissions in four-level GaAs/AlGaAs asymmetric quantum wells. The optical pump source is a CO₂ laser. Although this type of THz laser is able to work at room temperature its main drawback is the large dimensions of the optical pump source [95]. There are also some THz masers proposals. A THz spin flip maser is based on the population inversion between Zeeman-split levels, which flip their associated spin through tunneling [96]. Another THz maser proposal is based on optical phonon transit time resonance in bulk GaN [97]. Calculations show that these masers are able to work efficiently at 30 K.

2.3. THz generation/detection using nanodevices

The involvement of nanotechnologies in the realization of THz generation/detection devices is more than 10 years old. It started with the observation of the emission of THz electromagnetic radiation from an asymmetric coupled quantum well structure, which consists from a wide well (WW) and a narrow well (NW) separated by a thin potential barrier [98]. Since the coupled quantum wells are not identical, the interband transition frequencies have different values in the two wells denoted by ω_1 for the WW and by ω_2 for the NW. The THz radiation is due to the coherent oscillation of electrons between the two quantum wells. These oscillations in the coupled quantum structure occur when the lower electronic levels in the WW and the NW are aligned by applying a dc voltage; when alignment of the lower electronic levels is achieved, i.e. at resonance, the electrons become delocalized. At the bias value for which the resonance condition is attained for electrons, the LH and HH lower energy levels in the coupled asymmetric wells remain generally misaligned, so that the holes remain localized in the respective wells. In these conditions new bonding and antibonding eigenstates are created at resonance, with corresponding energies E_+ and E_- , respectively. These HH–NW and HH–WW energy states show a hyperbolic dependence on the applied field, intersect each other and have a minimum splitting at resonance. All these physical properties allow the preparation of an electronic wavefunction in the WW through the excitation of the coupled quantum structure with a fs optical pulse that has a frequency equal to ω_1 and a spectral content $\Delta\omega_1$ larger than the difference of antibonding and bonding eigenstates' energies and smaller than the difference of interband frequencies in the two wells, i.e. $(E_- - E_+)/\hbar < \Delta\omega_1 < (\omega_2 - \omega_1)$. The electron wavepacket is in these conditions a superposition of the two eigenstates and tunnels the two coupled quantum wells at

the frequency

$$\omega_{\text{THz}} = (E_- + E_+)/\hbar. \quad (33)$$

The oscillating wavepacket produces on its turn a time-varying polarization, which can be associated with the electromagnetic radiation of a Hertzian dipole, i.e. $E_{\text{THz}}(t) < \partial^2 P / \partial t^2$. In an asymmetric GaAs/AlGaAs/GaAs coupled quantum well structure, oscillations at 1.5 THz were observed at 10 K by exciting the structure with an optical pulse of 160 fs duration and a photon energy of 1.53 eV. The generated THz frequency cannot be tuned by changing the bias, since such a change will bring the aligned energy levels off resonance.

THz electromagnetic radiation can also be produced by charge oscillations in a single quantum wells. In GaAs single quantum wells structures, for example, separated by AlGaAs barriers, the charge oscillations originate in the quantum beats resulting from the LH and HH excitons. In contrast with the case of coupled quantum wells, in the case of single quantum wells the resulting THz frequency can be tuned in the range 1–3 THz by changing the applied bias, which changes the energy levels of excitons [99]. To observe THz due to charge oscillations the photon energy must exceed both LH and HH levels of the GaAs quantum well.

These initial successes in the development of THz devices based on quantum nanostructures were possible due to the amazing technological developments in the area of band-engineered semiconductors. Other THz devices and effects based on nanostructures can be imagined as well, one of the most beautiful being the generation of THz Bloch oscillations. Bloch oscillations are the result of the dynamics of electron wavepackets that propagate in periodic potentials in the presence of an applied electric field. The electrons undergo a succession of carrier accelerations due to the applied electric field, until the electron momentum satisfies the Bragg reflection condition from the periodic component of the potential and is reflected, followed by electron decelerations due to the electric field until it is reflected by the linear component of the potential, completing the cycle. The electrons oscillate at the Bloch oscillation frequency ω_B and are localized in periodic orbits being Bragg reflected on one side and reflected by the uniform electric field on the other. A quantum treatment of the above electron wavefunction dynamics shows that Bloch oscillations are the result of the quantum beat of Wannier–Stark states. Sixty-five years have passed between the theoretical discovery of Bloch oscillations and the experimental proof of their existence. The reason is that in bulk solids scattering phenomena destroy the coherence of Bloch oscillations. For the first time, Bloch oscillations with a spectral width within the THz range were observed in a superlattice consisting of 35 periods of a thick GaAs well (9.7 nm) located between two $\text{Al}_{0.3}\text{Ga}_{0.7}\text{As}$ barriers (1.7 nm) [100]. The entire superlattice structure is presented in Fig. 25. At a low reverse bias, strong coupling between quantum wells occurs and the electron and hole wavefunctions are delocalized producing energy minibands. The lowest electron and hole miniband widths are 19 and 2 meV, respectively. Increasing the voltage, the minibands split into a series of discrete levels that form a Wannier–Stark ladder. The THz Bloch oscillations were generated by exciting optically the superlattice with a 100 fs pulse at the wavelength of 802 nm,

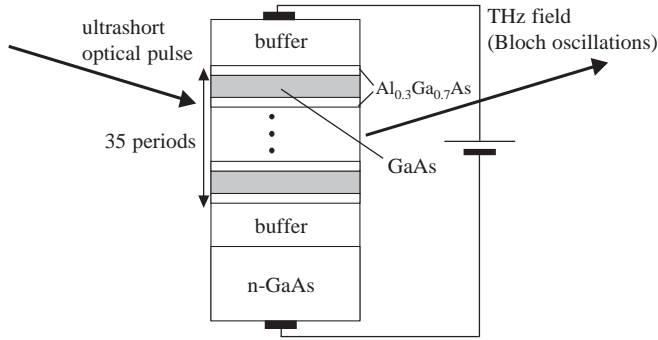


Fig. 25. THz Bloch oscillator.

which corresponds to the 0hh exciton transition. Bloch oscillations were observed at 15 K in the linearly tunable range of 0.5–4 THz, according to the Bloch frequency formula

$$\omega_B = eEd/\hbar, \quad (34)$$

where E is the applied dc electrical field, and d is the period of the superlattice. A review about optically induced Bloch oscillations tunable in the THz range can be found in Ref. [101]. Very recently electrically induced Bloch oscillations were theoretically predicted at THz frequencies through hot electron injection into the upper part of a superlattice miniband [102]. This injection mechanism shifts the region of negative conductivity towards higher frequencies, attaining 2–4 THz. In this way, the dc differential conductivity is positive and therefore suppresses the domain instability, while the high-frequency differential conductivity is negative above the Bloch frequency ω_B .

Despite the inherent beauty of the physical effects involved in THz generation based on charge oscillations, the devices described above show the same drawbacks as many other THz generating devices; more precisely, the THz emitted power is low even when the devices work at low temperatures. A possible solution to improve dramatically the performances of THz devices is represented by transistors with nanometer dimensions, named also nanotransistors or THz transistors.

The high electron mobility transistor (HEMT) represents a first category of such transistors. The cutoff frequency of the HEMT, given by $f_T \approx 1/2\pi t_i$, where t_i is the electron transit time, does not exceed 0.6 THz. This cutoff frequency could be enhanced towards 10 THz if the HEMT would work in a special operation mode when electron plasma oscillations are propagating in the HEMT channel. In such a channel electrons propagate ballistically and, when the sample length and the free path of electrons resulted from collisions with impurities and/or phonons are both greater than the electron free path resulting from collisions with other electrons, the entire 2D electron gas existing in the HEMT channel behaves like a frictionless fluid analogous with shallow water, which can be described by hydrodynamic equations [103,104]. In these conditions plasma waves are produced with a dispersion relation $\omega = v_P k$, where the plasma wave velocity $v_P = (eV_G/m_{\text{eff}})^{1/2}$ is of the order of

10^8 cm/s and V_G is the gate-to-channel voltage swing. The entire HEMT acts like a resonator for plasma waves at the resonance frequency v_p/L , with L the channel length; the quality factor of the resonator is given by $Q = v_p\tau/L$, where τ is the momentum relaxation time. When we have an ac short circuit at the HEMT source end the eigenmodes of HEMT plasma oscillations are odd harmonics of the fundamental plasma oscillation $\omega_{osc} = \pi v_p/2L$. Many THz devices working at room temperature such as resonant mixers, detectors or oscillators can be implemented using the principles described above. For example, for gate lengths within the interval 60–100 nm a HEMT THz oscillator is able to generate 1 mW within the THz range. A HEMT detector working in the plasma regime can exceed with 2–3 orders of magnitudes the responsivities of Schottky detectors, which are about 10^3 V/W. THz resonant mixers and multipliers can also be implemented.

Very recently, it was shown that self-oscillations of plasma could take place in HEMT-like heterostructures with tunneling or thermionic injection of electrons from the channel into the gate layer [105]. The plasma instability is possible due to the combination of plasma resonances with transit-time resonances of injected carriers in the gate layers. In this case the plasma dispersion equation is different from that given above, but plasma oscillations between source and drain of a AlGaAs/GaAs HEMT-like structure are still within the THz range when the gate length is of the order of 500 nm at room temperature.

Moreover, simple devices such as T-branch and rectifier diodes can be implemented and realized using the same concept of ballistic channels in AlInAs/InGaAs HEMT devices, where the ballistic transport is present at room temperature due to the extremely long electron free path, which is of about 100 nm at 300 K. In this way, multiplexors/demultiplexors are able to process THz signals [106].

A THz transistor able to switch 10^{12} times per second is now under development by Intel. It is a Si-based FET transistor that incorporates some new features compared to a classical FET transistor. For example, it has a new gate dielectric placed under the gate, a layer of oxide buried in the silicon substrate and a raised source and drain. The gate length is between 60 nm and 90 nm, i.e. it has a thickness of 3–5 atomic layers. For more details see the paper of Teixeira and other papers written by the Intel team at www.intel.com/research/silicon.

A room temperature THz transistor was recently realized [2]. This is a ballistic and tunneling GaAs static transistor with a 10 nm scale channel. The measured electron transit time was 2×10^{-14} s, i.e. 20 fs! The cutoff frequency is thus about 9 THz.

THz generation at very low powers was observed when two CW lasers emitting at different frequencies, such that the difference between them is located within the THz range, were focalized in the air-gap of a single tunneling microscope (STM) that consists of a sharp nanotip positioned a few nanometers above a metal ground. This is in fact a nanophotomixer (see Fig. 26), emitting THz radiation due to the nonlinear characteristics of the STM-like diode, which is analogous to a metal–insulator–metal (MIM) diode [107]. Such sharp nanotips can be realized using micromachining techniques applied to Si or GaAs; then, the nanotips are metallized. In connection with THz emission by a STM, it was theoretically demonstrated that resonant photon-stimulated field emission is able to generate signals up to 100 THz [108].

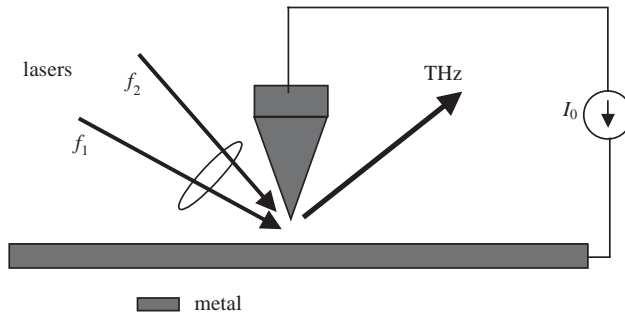


Fig. 26. THz nanophotomixer.

The latest trend in THz nanodevices is their implementation with the help of carbon nanotubes (CNT). Depending on the wrapping of a graphene sheet CNTs can be either metals or semiconductors with a bandgap that can be engineered by choosing a certain diameter of the tube, by applying a stress on the nanotube or by doping it. CNTs with a diameter varying between 10 and 50 nm could be the building blocks of many future THz devices. Schottky diodes and negative differential conductivity diodes with unprecedented performances compared to similar devices based on bare semiconductors or heterostructures were already simulated [109–111].

CNTs were used as field emitters generating current densities of 100–1000 A/cm² in a nanoklystron device designed to produce 3 mW at 1.2 THz [112]. An array of CNTs is a very efficient electron source for low-power and high-current densities. The entire reflex nanoklystron is made using Si micromachining techniques and is composed from two parts, which are sealed in vacuum. The entire vacuum microtube is very small; its dimensions do not exceed 100 μm . We have presented in Fig. 27 the THz devices based on CNTs described above.

A single-walled CNT (SWCNT)-based RTD able to overcome the maximum oscillation frequency attainable with RTD based on semiconductor heterostructures is represented in Fig. 28a. The SWCNT is a functional device allowing the creation of rectangular quantum wells beneath dc biased metallic gates whereas rectangular barriers are produced between them. The widths of the barriers given by the distance between the gate electrodes is taken as 10 Å and the well width determined by the length of the inner gate contact is 20 Å. The device described above is simulated with the method described in Ref. [113]. The dependence of the transmission coefficient and the transit time of the RTD on E are displayed in Fig. 28b for a (17,0) SWCNT with an effective mass of $0.216m_0$, where m_0 is the free electron mass, and for $V_1 = V_2 = V_3 = 0.8$ eV, considering the reference for the electron energy at the bottom of the well. The transmission coefficient takes significant values only around the two resonant energies of the quantum well: 0.193 and 0.72 eV. The transit times, however, for these two resonant energies are very different, 1.5×10^{-13} and 1.35×10^{-14} s, respectively. To have a very short transit time through the device, the contribution of the electrons tunneling through the lowest resonant state must be

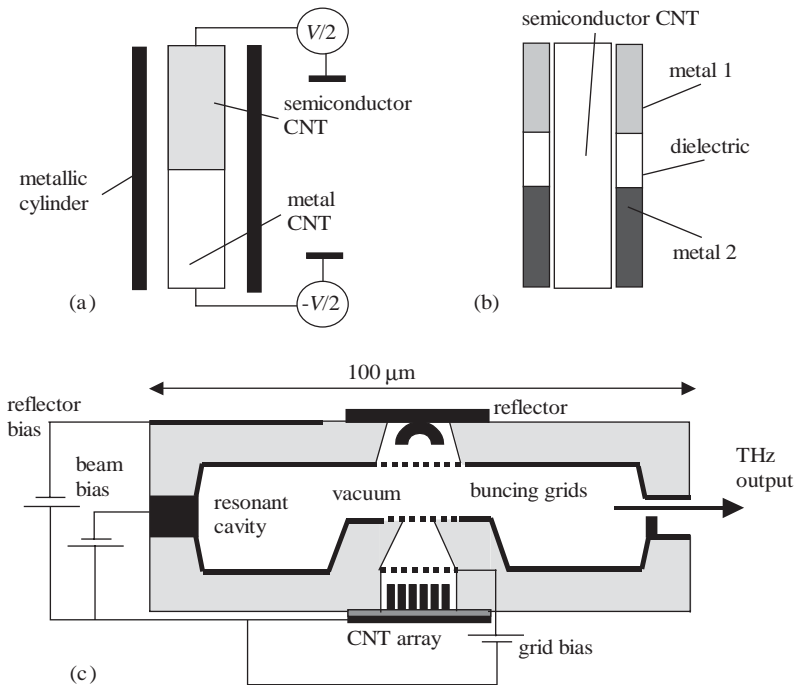


Fig. 27. THz CNT devices: (a) Schottky diode, (b) negative differential resistance diode, and (c) nanoklystron with a CNT array cathode.

suppressed. This cannot be done by controlling the position of the Fermi level in the emitter, for example, because enabling the electrons to reach the highest resonant level automatically implies that the electron states around the lowest resonant levels are occupied, and thus tunneling on the lowest resonant level automatically takes place. The only possibility to avoid this is to engineer the value of V_1 such that the electron states around the lowest resonant level in the well cannot be reached by electrons in the emitter region. The simplest way to do this is to raise the bottom of the conduction band in the emitter region above the lowest resonant level in the well. Considering again the energy reference at the bottom of the quantum well, the bottom of the conduction band in the emitter region can be raised, for example, with 0.35 eV above zero. The transmission and transit time dependences on E are in this case given in Fig. 28c for the situation when the bias along the SWCNT axis is absent (solid lines) or takes the value $V_{DC} = 0.5$ V (dashed lines); it was assumed that V_{DC} drops mainly across the RTD. From Fig. 28c it can be seen that the position of the highest resonant state in the quantum well shifts to lower energies when the SWCNT is biased, and the transit time at the position of the resonant state shifts also to lower values, i.e. it becomes even faster than 1.35×10^{-14} s, attaining the value of 10^{-14} s. A transit time of 10 fs, as that attained in this biased device, corresponds to a cutoff oscillation frequency of about 16 THz, two times higher than the cutoff frequency of

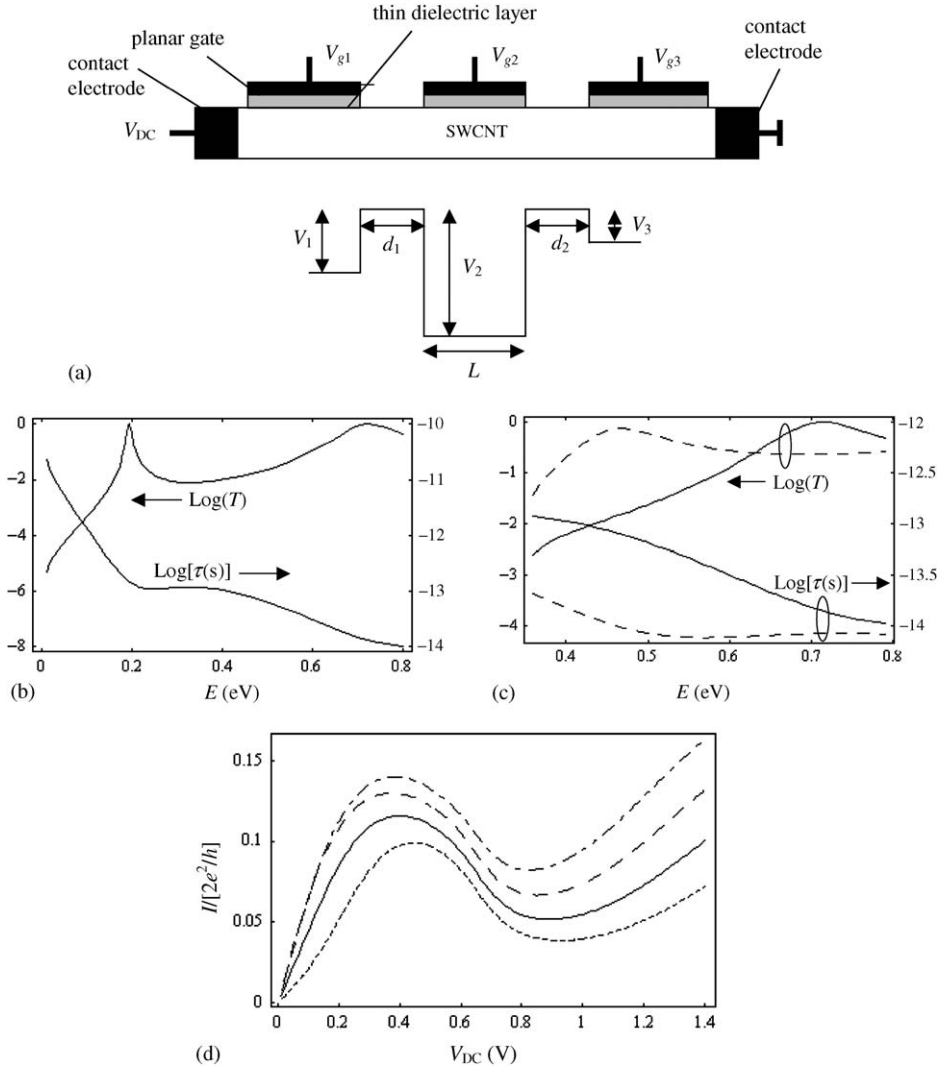


Fig. 28. (a) Schematic representation of a SWCNT-based RTD and its energy diagram. (b) Transmission coefficient and transit time energy dependence of a SWCNT-based RTD with $V_1 = V_2 = V_3 = 0.8$ eV and no applied bias. (c) Same as in (b) for $V_1 = 0.45$ eV and $V_2 = V_3 = 0.8$ eV (solid line: no bias, dashed line: $V_{DC} = 0.5$ eV). (d) Room temperature $I - V_{DC}$ characteristics for the structure in (c) with Fermi energy levels at 0.6 eV (dotted line), 0.65 eV (solid line), 0.7 eV (dashed line) and 0.75 eV (dashed-dotted line) measured from the bottom of the quantum well.

the THz ballistic transistor, which has a transit time of 20 fs [2]. The $I - V_{DC}$ dependence of the device was computed using the Landauer formula $I(V) = \int T(E)[f_L(E) - f_R(E)]dE$, where $T(E)$ is the transmission coefficient and $f_L(E)$ and $f_R(E)$ are the Fermi distributions of the left and right contact electrodes. The $I - V_{DC}$ dependence is displayed in Fig. 28d for four values of the Fermi level:

0.6 eV (dotted line), 0.65 eV (solid line), 0.7 eV (dashed line) and 0.75 eV (dashed-dotted line), at room temperature. These values of the Fermi energy level are calculated from the bottom of the conduction band in the well region; the value of 0.35 eV must be subtracted to obtain the values with respect to the bottom of the conduction band in the emitter region. A very pronounced region of negative differential resistance can be observed in all cases, assuring that oscillations with THz frequencies are produced along the SWCNT axis. An efficient THz oscillator should have a small negative differential conductance, i.e. a small $|\Delta I/\Delta V| = |(I_p - I_v)/(V_p - V_v)|$, where I_p , I_v , V_p , V_v are the peak and valley values of the intensity and voltage, respectively, a high $\Delta I\Delta V = (I_p - I_v)(V_p - V_v)$, i.e. a high output power, and a high I_p/I_v for a high signal-to-noise ratio. These conditions are contradictory. Therefore, the Fermi level can be chosen at 0.65 eV (0.3 eV above the bottom of the conduction band in the emitter region), for which $I_p/I_v = 2.23$.

The easiest way to couple the generated THz frequency to the propagation media is through quasi-optically means. Therefore, the metallic electrodes through which the voltage V_{DC} is applied throughout the structure have the shape of bowtie antennas, the bias being applied on the two arms of the antenna. These antennas radiate the THz power into free-space if V_{DC} is located in the negative differential resistance region of the $I - V_{DC}$ characteristics. The bias value of 0.5 V used in the simulations of Fig. 28c lies within the negative differential region of the SWCNT-based RTD. The condition of oscillation of the SWCNT-based RTD is $R_N + R_C + R_A < 0$, where R_N is the negative resistance of the RTD, R_C is the contact resistance and R_A is the radiation resistance of the bowtie antenna. This condition is satisfied for $R_C = 6 \text{ k}\Omega$ and $R_A = 80 \Omega$, and for a value $R_N = -99.2 \text{ k}\Omega$ determined from Fig. 28d for the Fermi level value of 0.65 eV. Thus, the device can indeed oscillate at a cutoff (intrinsic) frequency of oscillations of $f_{RC} = [G/(R_C + R_A) - G^2]^{1/2}/(2\pi C_{RTD})$, where C_{RTD} is the capacitance of the SWCNT-based RTD. This capacitance is $C_{RTD} = 100 \text{ aF}/\mu\text{m}$, which for a 4 nm long structure gives 4 aF. In these conditions $f_{RC} = 16.4 \text{ THz}$, a value that is very close to the oscillation frequency estimated from the transit time computation. The output power of the SWCNT-based RTD oscillator, equal to $\Delta I\Delta V = (I_p - I_v)(V_p - V_v)$, is found to be $2.5 \mu\text{W}$ using the data from Fig. 28d. In order to increase the THz power an array of equally spaced SWCNT-based RTD devices can be implemented, where the distance between two antennas loaded with SWCNT-based RTD is $c/2f_{RC}$. Then, the radiated power in the directions for which the interference between the radiations emitted by the antennas is constructive increases proportional to N^2 , where N is the number of the radiating elements. So, an array containing tens of bowtie antennas loaded with SWCNT-based RTD can produce an output power of a few milliwatts in the frequency range of 1–16 THz.

3. THz propagation

There are two distinct ways to propagate THz fields: (i) quasi-optical techniques and (ii) guided-wave techniques. The most encountered is the quasi-optical

propagation, which consists in the transmission of THz fields in free-space between the emission and reception planes. This is possible when the electromagnetic beam is collimated and is not seriously distorted by diffraction. The quasi-optical method was for many years the only solution for THz field propagation since guided-wave methods based on metallic or dielectric waveguides have major drawbacks in the submillimeter frequency range. The waveguides have very high losses, which increase with (frequency)² and require extremely tight mechanical tolerances. In a metallic rectangular waveguide the losses at 1 THz are about 0.4 dB/cm. The large majority of dielectrics, with the notable exception of Si, have large absorption coefficients in the THz range. Only recently the micromachining techniques were able to realize quite thin substrates on which THz propagation experiences losses comparable to those obtained in quasi-optical techniques.

Therefore, quasi-optical techniques are very spread in the THz range and a THz setup has many similarities with an optical setup. THz quasi-optical techniques are best described by geometrical optics and paraxial approximation. Since the amplitude distribution transverse to the direction of propagation of many transmitting/receiving THz antennas shows a Gaussian shape, the Gaussian optics based on the ABCD matrix calculation is applicable to THz quasi-optical techniques. A review of quasi-optical techniques can be found in Ref. [114], while the Gaussian optics is very well explained in Ref. [115]. A 2×2 ABCD matrix is assigned to each quasi-optical component (lens, filter, plate, etc.) and to each free-space distance separating them. Then, the product of all ABCD matrices provides the transfer function of the entire quasi-optical system, thus allowing a complete description of the propagated beam properties. There are even analytical techniques able to extend this method in the case of non-paraxial THz beams, i.e. beams with a divergence generally exceeding 19° , using beam-mode transfer matrices [116].

Despite the similarities with optics, there are some specific quasi-optical THz devices used for beam shaping and processing that can differ considerably from their optical counterparts. For example, wire grids are used as polarizers able to rotate significantly the polarization plane of an incoming THz beam without any distortion. Wave dielectric plates of various thicknesses are used as phase shifters. Some quasi-optical components are displayed in Fig. 29 together with their transmission functions. THz filters are represented in Figs. 29a–c, while in Fig. 29d a Fabry–Perot cavity is displayed, which can also play the role of a filter. All these quasi-optical components are based on 2D periodic arrays of metallic wires, metallic plates or slots; using a modern terminology all are photonic bandgap devices (PBG). Simple formulas describe their basic parameters. For example, in the case of the resonant wire grid filter depicted in Fig. 29c, the length of the cross-like slot is $L = \lambda_0/2.1$, while the spatial period between two slots is $P = \lambda_D/(1 + \sin \theta_i)$, with λ_D the longest wavelength at which diffraction can occur and θ_i the incoming THz beam angle. Its transmission characteristic has a Lorentzian shape given by

$$T(f) = \alpha / [(f - f_0)^2 + \alpha^2], \quad (35)$$

where $f_0 \cong \pi c/L$ is the resonant frequency and α is the half-power width of the resonance profile [117].

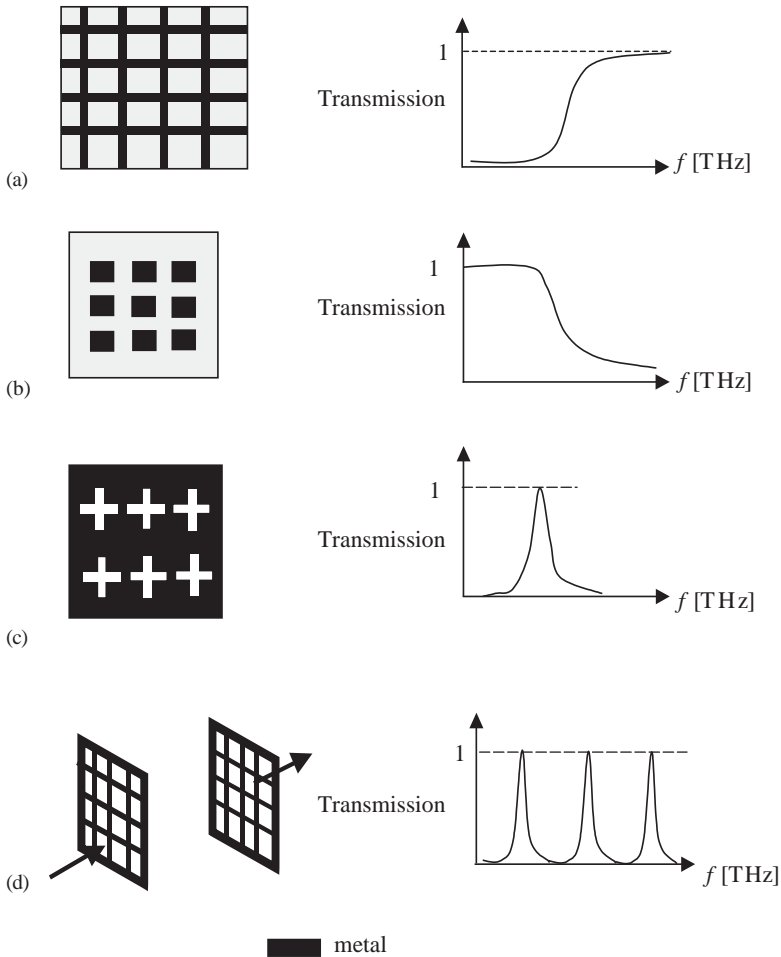


Fig. 29. Quasi-optical THz devices: (a) wire grid filter, (b) capacitive-plate filter, (c) resonant wire grid band-pass filter, and (d) Fabry-Perot cavity.

Diplexers are multi-port quasi-optical devices, which combine two or more signals, e.g. the incoming THz signal and a local oscillator. Martin-Puplett polarization rotating interferometers are used for such purposes [57].

The THz waveguided propagation has boosted in the last years due to micromachining techniques able to process semiconductor substrates with micrometric thicknesses. This is the only way to reduce drastically the large losses encountered in any dielectric substrate at THz frequencies.

The micromachining consists in removing a part of a bulk substrate or of a thin film using various etching techniques. An ideal candidate for micromachining is silicon, which has very good mechanical properties and a low absorption at THz frequencies. Since Si can be micromachined using usual etching technologies

borrowed from the semiconductor technology, Si micromachining is the most frequent procedure utilized to obtain quasi-optical THz devices such as lenses, antennas, or filters. The micromachining of GaAs or InP is also possible and desirable for THz applications since III–V semiconductor compounds are employed in THz devices such as photoconductor emitters/receivers and THz semiconductor lasers. CPW on micromachined semiconductor substrates should be able to drive to an antenna the emitted power from a THz semiconductor laser. An array of a few THz semiconductor lasers connected between them by micromachined CPW lines terminated with slot antennas will be able to emit an output power of tens of mW. Micromachined techniques are intensively used in THz electronic devices as, for example, the substrateless technique described in Section 2.2.3. III–V semiconductors or heterostructures based on them show piezoelectric, piezoresistance and thermoelectric properties due to the polar character of the bonding between different atoms in the unit cell. These properties could be further used for THz MEMS devices.

The various etching shapes obtained by applying different techniques are represented in Fig. 30. The etching techniques are divided into two large categories: wet or chemical (presented in Figs. 30a and b) and dry or plasma etching (Fig. 30c). The aim is to obtain controllable, high-precision shapes with low roughness after the etching process. In the case of Si, GaAs or InP anisotropic etching and plasma etching are used. Perfect vertical walls can only be obtained using plasma etching methods. More sophisticated methods, based on laser etching or synchrotron radiation (called LIGA) can be employed to realize perfect walls or various semiconductors shapes.

There are two large types of micromachining techniques. In the first technique, called bulk micromachining, the back of a wafer is etched in order to obtain a prescribed mechanical structure on its top. A simple but very important example is shown in Fig. 31: the fabrication of a micromechanical membrane. Nowadays, very large membranes with surfaces of $2 \times 2 \text{ cm}^2$ and a thickness of $1 \mu\text{m}$ can be obtained by using chemical or plasma-etching methods. In the case of bulk micromachining

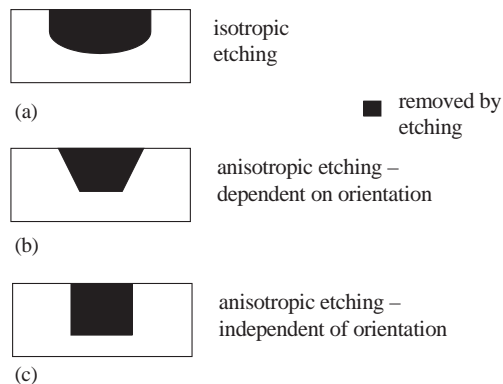


Fig. 30. Basic micromachined shapes using different etching techniques.

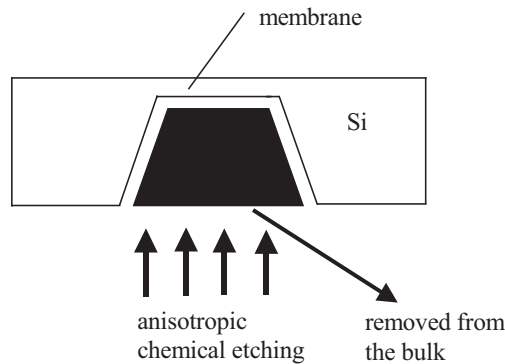


Fig. 31. Illustration of bulk micromachining.

Table 1
Etch stop techniques for chemical etching procedures

Name of the etch stop technique	Description	Accuracy
Time stop	The etch is stopped after a prescribed time	Low
p ⁺	A thin p ⁺ layer remains after removing Si in combination with EDP etchants	High
Electrochemical (photovoltaic, galvanic, etc.)	The thickness is obtained through epitaxy. An etch stop is realized through a p-layer grown on a n-type substrate	Very high

the precision and the desired shape of mechanical structures realized at the micro or nano-scale is determined by the etching-stop techniques. Some etching-stop techniques are summarized in Table 1.

The second micromachining technique is surface micromachining. In this technique, MEMS or NEMS are realized by successive thin film depositions on a common substrate, followed by the selective etching of one of these thin deposited layers, called the sacrificial layer. The realization of a cantilever in this technique is schematically represented in Fig. 32. In the Si technology the sacrificial layer can be of polysilicon or different types of resists, while the mechanical layer (located over the sacrificial layer) can be of silicon nitride, silicon dioxide, gold or aluminum. The pair mechanical-sacrificial layers is selected in such a way that after a specific etching the mechanical layer remains intact while the sacrificial layer vanishes completely.

The applications of micromachining techniques for THz domain started in 1980 when a tapered-rod antenna was realized for a wavelength of 120 μm by using anisotropic etching of the silicon rod supported on a silicon dioxide membrane on which a bismuth bolometer was patterned [118]. Many THz devices were

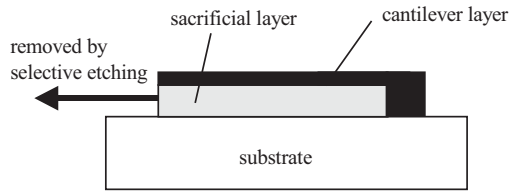


Fig. 32. Illustration of the surface micromachining technique.

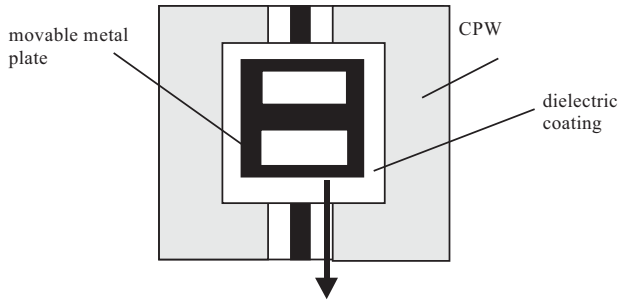


Fig. 33. MEMS sliding planar backshort.

subsequently realized: a slot endfire Vivaldi-like antenna at 802 GHz on a $1.75\ \mu\text{m}$ silicon nitride membrane, a 16×16 THz horn array forming a CCD-like imaging array at 802 GHz [18], waveguides and mixers [8,9] multipliers and receivers [84]. There are also two other reviews of THz micromachined propagating and radiating devices [119,120] such as waveguides, lenses, filters, CPWs and other transmission lines, as well as antenna arrays, which are very useful in the understanding of why micromachining techniques are so attractive for THz technologies.

Moreover, even movable microfabricated translators able to tune THz transmission lines were realized using surface micromachining techniques [120]. An example of such a movable translator is a sliding planar backshort, which consists of a rectangular metal plate that translates linearly along a CPW transmission line, varying in this way its electrical length (see Fig. 33). This MEMS device was used to tune a 620 GHz detector circuit.

A new trend in propagation of THz fields is the guiding of THz pulses. We have to point out that all THz devices described above are suitable only for CW THz fields. Recently, however, THz pulse propagation in single-mode waveguide sapphire fibers with a diameter of $325\ \mu\text{m}$ was experimentally tested [121]. Similar experiments were performed in $240\ \mu\text{m}$ diameter cylindrical stainless steel waveguides and in parallel-plate copper waveguides [122,123]. In the case of sapphire fibers, THz pulses were reshaped due to the dispersion and absorption encountered in the dielectric waveguide. Very low-loss, but very dispersive THz propagation was observed in the case of the THz metallic cylindrical waveguide. For the first time, dispersionless, and low-loss propagation of an incoming $0.3\ \text{ps}$ THz pulse was observed in the bandwidth $0.1\text{--}4\ \text{THz}$ for a length of $25\ \text{mm}$ via parallel-plate waveguide.

4. THz detection

THz detection is a quite difficult task since the power of emitted THz signals is weak. Moreover, due to the low photon energies of the THz band (1–10 meV) ambient thermal noise prevails over the THz signal and thus cooling of detectors is very often required. Other detection configurations that increase the signal-to-noise ratio, such as the heterodyne detection, are frequently used either at room temperature or cooled.

4.1. Detection of ultrashort electrical pulses

Ultrashort electrical pulses with a spectral content within the THz frequency range, produced using various physical principles (see Section 2.1), are detected using mainly two methods. The first method uses a gated photoconductive antenna and is called photoconductive sampling or, briefly, PC sampling. The second method is based on the detection of the polarization change of an optical probe beam produced by the THz field when both fields are applied on an electro-optic crystal; this method is called free-space-electro-optic sampling FS-EOS. The configurations of both detection schemes are presented in Fig. 34.

In the case of PC sampling the charge generated at the antenna terminals is [124]

$$q(\tau) = \int v(t)g(t - \tau) dt, \quad (36)$$

where $v(t)$ is the voltage across the photoconductive gap, given by

$$v(t) = \int H(\omega)E(\omega) \exp(i\omega t) d\omega. \quad (37)$$

Here $E(\omega)$ is the Fourier transform of the incident electric field pulse $E_{\text{THz}}(t)$ and $H(\omega)$ is the transfer function of the antenna, i.e. the ratio between the voltage induced at the antenna terminals and the incident electric field, both represented in

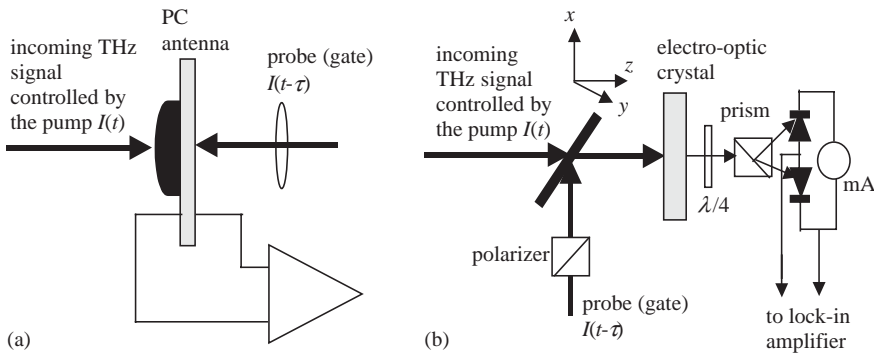


Fig. 34. Ultrashort electrical pulse detection. (a) PC-sampling, (b) FS-EOS.

the frequency domain. The conductance is given by

$$g(t) = \int I(t') \{1 - \exp[1 - \exp(t - t')/\tau_{\text{rel}}]\} \exp[(t - t')/\tau] dt'. \quad (38)$$

From Eq. (38) it follows that the PC sampling output signal is dependent on the incident field $E_{\text{THz}}(t)$, but also depends on the momentum relaxation time τ_{rel} and the carrier lifetime τ of the PC substrate. It was experimentally found that when THz detection is performed with a short dipole without a substrate lens [124], $H(i\omega) = 1$, and so $v(t)$ becomes directly proportional to the incident THz signal $E_{\text{THz}}(t)$. When the THz detector consists of a short dipole with a substrate lens, $H(i\omega) = i\omega$.

The FS-EOS uses the linear electro-optic effect in an EO crystal excited by an optical probe field and the THz field. Both fields propagate in the same direction but have different polarizations. For example, if z is the propagation direction, the optical probe is polarized at 45° in the (x, y) plane perpendicular on z due to birefringence of the EO crystal, while the THz field is perpendicular on the y axis. Since the electro-optic effect is practically instantaneous at the THz scale, the output of a FS-EOS detector is directly proportional to $E_{\text{THz}}(t)$ [125]. Due to the presence of the THz field a phase retardation $\Delta\varphi$ of the optical field is produced over the distance dz , which is strongly dependent on the electro-optic crystal type and orientation. FS-EOS uses different types of electro-optic crystals: (i) uniaxial crystals like LaTiO_3 or LiNbO_3 , or (ii) isotropic crystals like (1 1 0) ZnTe with a zinc-blende structure. ZnTe is a material for which a high signal-to-noise ratio was obtained. For ZnTe the phase retardation is given by

$$\Delta\varphi(\tau) = (\omega/c)n_0^3r_{41}E_{\text{THz}}(\tau)dz = \text{const}_{\text{ZnTe}} \times E_{\text{THz}}(\tau)dz, \quad (39)$$

where ω is the optical frequency of the probe and r_{41} is the electro-optic coefficient. From the above relation it follows that the THz field obtained after propagating over a length L in a ZnTe crystal, material with small absorption and a refractive index difference of $\Delta n = n_{\text{THz}} - n_{\text{opt}} = 0.22$, is

$$E_{\text{THz}}(\tau) = \Delta\varphi(\tau)/(L \times \text{const}_{\text{ZnTe}}). \quad (40)$$

Thus, measuring the phase change we are able to determine the time variation of the THz signal $E_{\text{THz}}(t)$.

Both detection methods, which are coherent methods, were compared using the same laser power modulated by an acousto-optic modulator. At low-frequency modulation the PC sampling method shows a better signal-to-noise ratio and sensitivity, for an identical received THz average power. Increasing the modulation frequency over 1 MHz, the performances of the FS-EOS method become comparable, i.e. the signal-to-noise ratio of FS-EOS becomes greater than 10^4 [126]. However, FS-EOS is able to detect signals in a huge bandwidth 100 GHz–37 THz [127], while in the PC sampling method the bandwidth is limited to 3–4 THz due to antenna parameters.

4.2. CW THz heterodyne detection

The most sensitive receivers at microwave, millimeterwave and THz frequencies are based on the heterodyne principle, which consists in mixing of two signals, the incoming THz CW signal and the local oscillator (LO) signal. The LO has a fixed output power that should be much greater than the power of the incoming signal. The LO frequency is also different from that of the received signal. The heterodyne process is realized by a nonlinear device, named mixer, which has an output signal with a frequency proportional to the difference between the frequencies of the incoming THz signal and the LO; the frequency of the output signal is called intermediate frequency (IF). Heterodyne receivers can be described by a series of parameters, but the most encountered one in the THz range is the receiver noise temperature $T_R = T_{\text{mixer}} + LT_{\text{IF}}$. Here the indices indicate the noise contribution of the mixer and the IF first amplifier stage, respectively, and L is the mixer conversion loss.

Room-temperature heterodyne receivers are based on Schottky diodes, characterized by strong I – V and C – V nonlinear characteristics. In Schottky diodes operating at moderate bias values the I – V and C – V characteristics are well-known: $I = I_{\text{sat}} \exp[(V/nV_T) - 1]$ and $C = C_0/(1 - V_T/V_D - V/V_D)^{1/2}$, where n is the ideality factor, and V_D and V_T are the flat-band voltage and the thermal voltage, respectively.

However, the above expressions for the I – V and C – V characteristics are not valid at THz frequencies, because the operating point is near the flat-band voltage ($V - V_D < 3V_T = 3k_B T/e = 80$ mV at room temperature). The corresponding expressions of these characteristics at THz frequencies are, respectively [128]:

$$I = I_{\text{sat}} \exp(V_D/nT)/2 \sinh[(V_D - V)/nV_T], \quad (41)$$

$$C = \frac{C_0 \{1 - \exp[-(V_D - V)/V_T]\}}{\sqrt{1 - V/V_D - (V_T/V_D)\{1 - \exp[-(V_D - V)/V_T]\}}}. \quad (42)$$

At THz frequencies the planar Schottky diodes, which are based on GaAs, InP or semiconductor heterostructures, have submicronic dimensions, the anode diameter varying between 0.2 and 0.5 μm . Recently, a 2.5 THz monolithic mixer consisting of a GaAs Schottky diode placed between an input and an output low-pass filter was demonstrated, the filters decoupling the high frequency signals from the dc bias. The IF signal was generated using the membrane technique described in the previous section. The GaAs membrane was 3 μm thick and the anode area of the diode was $0.2 \times 1 \mu\text{m}^2$ [129]. The LO, which was a gas laser at 2.522 THz with a power of 3–5 mW, was injected in the mixer together with the 2.5 THz signal through a Martin–Purpeltt diplexer. The insertion loss was –17 dB giving a receiver noise temperature of 9000 K.

Much lower noise temperatures are obtained using cooled heterodyne receivers based on superconducting devices. These heterodyne receivers are based on SIS (superconductor–insulator–superconductor) tunnel junctions that have a pronounced nonlinear I – V characteristic due to tunneling of quasiparticles in the

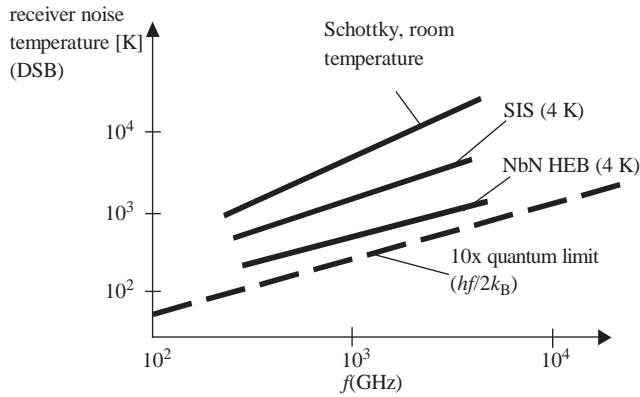


Fig. 35. Receiver noise temperature for heterodyne receivers in the THz range.

superconducting gap, and operate up to a cutoff frequency $f_c \cong 150 T_c$, where T_c is the critical temperature at which the transition towards the superconducting state takes place. Typical junctions are based on superconductors such as Nb ($T_c \approx 9$ K) or high-temperature superconductors (HTS) such as YBCO ($T_c = 100$ K). Even for Nb the cutoff frequency is greater than 1.3 THz. The main drawback of the SIS heterodyne receiver, namely its low operating temperature, is overcome by the fact that the required LO power is one order of magnitude lower than that for THz receivers based on Schottky diodes. Even lower receiver noise temperatures are obtained using hot electron bolometer (HEB) mixers. The receiver noise for the three types of mixers is represented in Fig. 35 [130].

HEB mixers are based on the heating of a superconducting microbridge with a THz radiation such that the corresponding electron temperature is higher than the phonon temperature of the device. The resistance of the bolometer is dependent on the electron temperature, the detected voltage being proportional with the THz power when the bolometer is dc biased. The short relaxation time of heated electrons (about 10 ps) allows a very fast variation of the microbridge resistance at IF up to several GHz. The high-speed operation makes HEB mixers the most sensitive THz heterodyne receivers, their noise temperature almost approaching the quantum limit (see Fig. 35). The nonlinear I – V curve necessary for mixing originates in this case in the electron heating of the microbridge, which experiences the superconducting transition. In Fig. 36 we have represented the three I – V characteristics of THz heterodyne receivers.

There are two main types of HEB mixers [131]. The first type, named “phonon-cooled” or “lattice-cooled”, is based on the strong electron–phonon interaction and the fast phonon escape time. In this type of HEB the relaxation time is strongly dependent on the film thickness. The maximum IF frequency is proportional to $1/\tau_{e-ph}$, where τ_{e-ph} is the electron–phonon relaxation time. If we desire an IF bandwidth of 10 GHz, the thickness of the superconducting microbridge must be less than 6 nm. Microbridges from Nb, NbN, Al, or YBCO have thus submicronic or

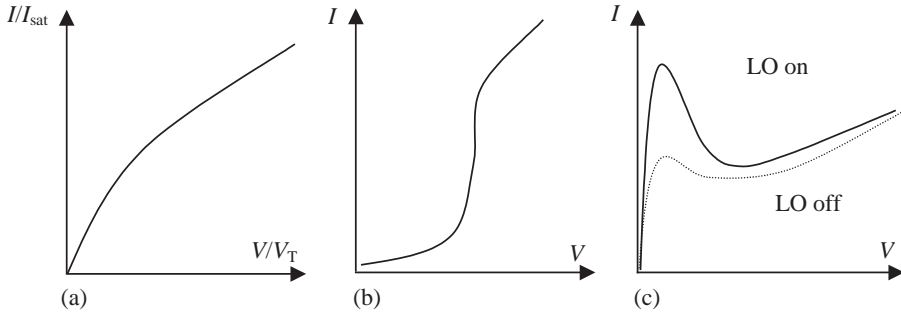


Fig. 36. I – V characteristics of nonlinear elements on which THz heterodyne receiver are based: (a) Forward biased Schottky diode, (b) SIS, and (c) HEB.

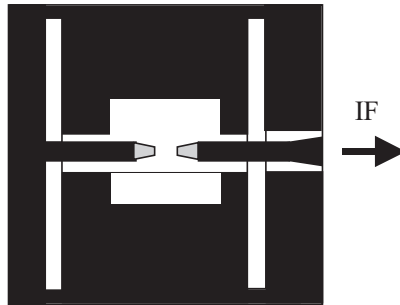


Fig. 37. HEB mixer with CPW twin slot antennas.

nanometric thicknesses; for example, in the case of NbN film the thickness is 3–4 nm if the first type of HEB is implemented. The HEB can be positioned at the center of a twin-slot CPW antenna [132] (Fig. 37).

The second type of HEB mixers, named “diffusion cooled”, is based on the cooling mechanism produced by the out-diffusion of hot electrons to a heat sink. This is realized by connecting the ends of the superconducting microbridges to normal metal pads.

Both types of the HEB mixers can be described by the same equations [133]:

$$-K \frac{d^2 T_e}{dx^2} + (C_e / \tau_{e-ph})(T_e - T_0) = j^2 \rho_n + P_{THz}, \quad (42a)$$

$$-K \frac{d^2 T_e}{dx^2} + (C_e / \tau_{e-ph})(T_e - T_0) = P_{THz}, \quad (42b)$$

where T_e is the electron effective temperature, C_e is the electron specific heat, K is the thermal conductivity, j the bias current density, ρ_n the mixer resistivity in normal state and P_{THz} the absorbed LO power/unit volume. The first equation, Eq. (42a), is valid inside the hot spot, while Eq. (42b) describes the electron temperature outside this spot.

4.3. Direct THz detection using micro and nanodevices

Micro- and nanotechnologies have boosted many areas of applied sciences and, in particular, the THz detection devices. In Fig. 38 we have presented a bolometer working up to 3 THz, realized using MEMS techniques [134]. The bolometer is a square sheet of bismuth with a length greater than 1.5λ evaporated on a thin dielectric membrane, SiO_2 (thickness 700 nm)/ Si_3N_4 (thickness 350 nm)/ SiO_2 (thickness 450 nm). A 20 element array was implemented to detect with the required precision the beam profile of a FIR laser.

A bolometer is able to measure only the power of the incoming radiation. Using the conceptions of MEMS techniques it was shown very recently [135] that an array of micromachined nanosized Fabry–Perot-like cantilevers can be used to sense simultaneously the power and the frequency of the THz field. This device is based on the electromagnetic actuation of micromachined cantilevers in the THz range. The device, which is a combination of a cantilever and a Fabry–Perot resonator, is schematically represented in Fig. 39. The THz field bends the entire microstructure, producing an additional tunneling current, which flows between the tip and the

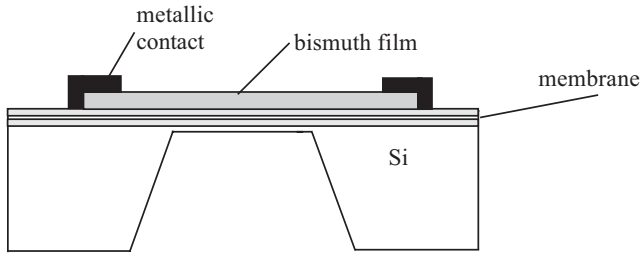


Fig. 38. THz bolometer based on MEMS technology.

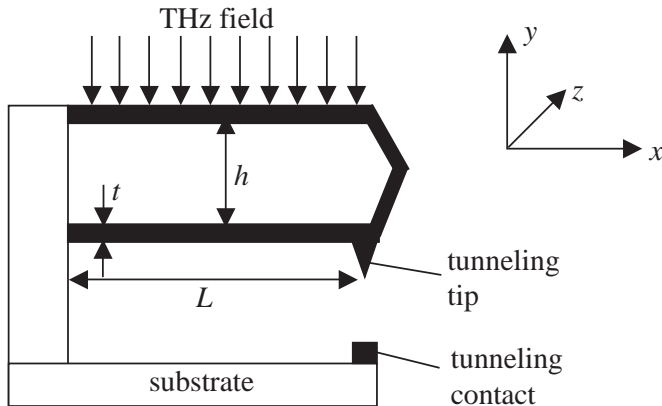


Fig. 39. Fabry–Perot-like cantilever for THz power and frequency sensing.

contact below it. Due to the exponential dependence of the tunneling current on the cantilever deflection even small deflections of about 1 Å produce large changes in the current (greater than an order of magnitude).

A THz field that excites uniformly the microstructure presented in Fig. 39 will deflect it with the amount $\delta = RPL^3/(6cEI)$, where R is the reflectivity of the entire microstructure, P the incident power, $I (= Wt^3/6 + Wth^2)$ the moment of inertia, and L the length of the arm of the Fabry–Perot like cantilever. To have a large deflection it is necessary to have a large L , a small thickness t and a small width W . The reflectivity of the microstructure is given by

$$R = \frac{4R_0 \sin^2(2\pi fh/c)}{(1 - R_0)^2 + 4R_0 \sin^2(2\pi fh/c)}, \quad (43)$$

where R_0 is the reflectivity of one of its arms, i.e. of a slab with a thickness t . A large R_0 can be attained for metallic arms, whereas a large R implies additionally a high h . If the incident THz field is normal to the microstructure, the reflectivity (and hence the deflection) is independent on polarization; otherwise polarization effects of the THz field should be considered. The incoming THz power is determined by measuring the variation of the tunneling current that is produced by the deflection δ . The incident power P is not the power emitted by the THz source, P_s , but is the fraction of this power incident on the Fabry–Perot-like cantilever, i.e. $P = P_s A_c/A_f$, where $A_c = LW$ is the cantilever area and A_c the focalization area. A power of $P_s = 15$ mW, for example, can be focalized on an area of 3×0.3 mm², so that on a cantilever with $L = 3$ mm, $W = 0.1$ μm, $t = 0.01$ μm, $h = 8$ μm and $R_0 = 0.9$, the incident power is $P = 5$ μW. This power produces a deflection of about $\delta = 140$ Å at a frequency of 1.5 THz for a structure made of gold with $E = 80$ GPa. Recently, it was demonstrated that large-scale metallic nanowires can be grown in the pores of silica gel. Although the length of the device in the example above seems at first to be too long, we must take into consideration that the device is not a simple cantilever, but a microstructure with a much higher inertia. Therefore, under the action of its own weight, the deflection of the microstructure is $\xi = qL^4g/8EI$, where q is the mass per unit length and $g = 9.8$ m/s². ξ is approximately 45 nm for this device compared to 350 nm for a simple cantilever with the same dimensions as an arm of the Fabry–Perot-like cantilever structure. With such an arrow a simple cantilever will obviously break under the action of its own weight.

Since the deflection is proportional to the incident power and the measured tunneling current depends exponentially on the deflection, we have $I = I_0 \exp(KP)$, with I_0 determined by the applied bias and by the distance between the Fabry–Perot-like cantilever and the metallic tip. A device sensibility independent on the biasing conditions can be defined as $\partial \ln I / \partial P = K = (2m_0\phi)^{1/2} RL^3/(3cEIh)$, sensibility which is independent on the incident power, and which has the value 28.8 μW^{−1} for the Fabry–Perot-like cantilever in the example above.

To measure the wavelength an array of such Fabry–Perot-like cantilevers is needed, with h varying linearly along the array. For an array of N cantilevers along the z direction and separated by dW , the distance between the arms of the j th Fabry–Perot-like cantilever is $h_j = h_0 + A[(j - 1)(W + dW) + W/2]$, $j = 1, 2, \dots, N$ with A ,

h_0 constant parameters. Since the total reflection coefficient is periodic with h , taking maximum values at $h_j = (2m + 1)c/4f$ and minimum values at $h_j = mc/2f$, the frequency of the THz source can be determined monitoring the position in the array for which the reflection coefficient is minimum and/or maximum (in simple metallic cantilevers the reflectivity does not depend on its thickness.). The resolution in the bandwidth 1.2–58 THz is $\Delta f/f \cong 10^{-3}$ in the example considered here.

Semiconductor heterostructures play also an important role in THz detection. For example, a HEB bolometer detector and mixer was proposed using the nonlinearities provided by a heated 2D electron gas medium [136]. This is a HEB of the second type, where the electrons are cooled by diffusion into the contact. For a device that is $0.8 \mu\text{m}$ long, the time constant is 1 ps and the responsivity is 3000 V/W. At the operating temperature of 77 K, with a 100 GHz as IF and a $1 \mu\text{W}$ LO, the receiver noise temperature is 1000–2000 K at 1 THz. HEMT transistors are also used to detect THz radiation for a constant drain bias when plasma waves are launched in the short transistor channel. A good sensitivity was obtained when a HEMT structure, biased so that the drain–source current has a constant value $I_{\text{DS}} = 0.1 \text{ mA}$, was illuminated with a 2.5 THz CW beam [137].

MSM interdigitated photodetectors can be used to detect THz radiation when the widths of the metallic fingers and of the space between them have submicronic dimensions (25–900 nm). The Schottky photodetector is realized on a 200 nm thick GaAs/AlGaAs substrate, the later being used for carrier absorption. The MSM device is laterally illuminated by the THz beam (a waveguide-like excitation of the absorbing layer) to obtain a maximum quantum efficiency [138].

A latest trend in THz detection is the single-photon detection. This was already accomplished using a nanodevice—a single-electron transistor (SET)—at an operating temperature of 50 mK. The SET is made from two parallel quantum dots (see Fig. 40) [139]. One of the dots is coupled to a dipole antenna, which is illuminated by the THz radiation. Inside this dot an electron–hole plasma is formed, which produces a photomultiplication effect (10^8 – 10^{12} electrons/photons) that, on its turn, shifts the conductance of the other dot due to electron tunneling. The nanodetector has a sensitivity 0.1 photons/ 0.1 mm^2 . The noise equivalent power NEP is $10^{-17} \text{ W (Hz)}^{-1/2}$, three orders of magnitude better than any bolometer.

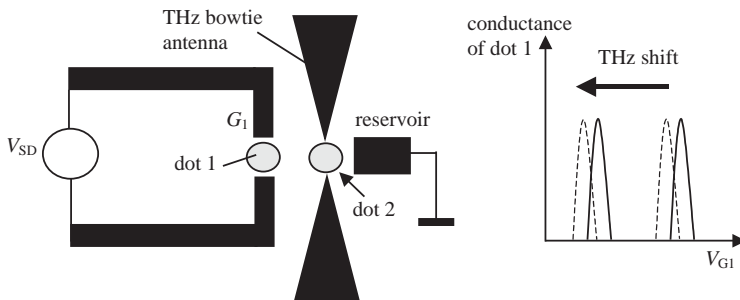


Fig. 40. THz SET detector.

5. Terahertz main applications

There are an increasing number of papers dealing with THz applications. Their number exceeds by far the number of papers dealing with the thorny problems of THz devices for emission or detection. Since the applications of THz are so well represented in the literature, we mention here only briefly the main areas where THz fields play a major role, underlining the physical problems encountered in each application.

The main two applications in which THz fields are involved are THz spectroscopy and THz imaging. These applications have contributed to a better knowledge of condensed matter, material properties and biology.

The most common THz spectroscopy method is based on time domain techniques, which employ either photoconductive or electro-optical methods for emission (see Sections 2.1.1 and 2.1.3) and detection (see Section 4.1). The setup for THz time domain spectroscopy (TDS) in a transmission configuration is realized by placing a sample between the THz emitter and receiver, the THz radiation passing through it. There are some important advantages of THz TDS:

- (i) Both photoconductive and electro-optical detection methods are coherent time-gated detection methods that detect the electrical field and not its intensity.
- (ii) The system works at room temperature because the noise background, which is stronger than the THz signal, is cancelled by averaging through time sampling and lock-in detection. This is possible because the polarization of the background noise is randomly distributed, while the THz signal has a predetermined polarization. In this way, high SNR are obtained (see Section 4.1), which exceed by orders of magnitudes the performances obtained with bolometers.
- (iii) The amplitude and phase of the detected THz signal, which results from the interaction of the emitted THz signal with the sample, are available. Using either analytical or numerical techniques the real and imaginary part of the dielectric permittivity are then available in a large frequency range.

Taking into account these important advantages it was believed that TDS will surmount in many ways the conventional spectroscopic method used in the THz range of frequencies, i.e. the Fourier-transform infrared (FTIR) spectroscopy. The FTIR spectrometer has as a source of radiation an incoherent arc lamp and is based on the two-beam interferometry principle. In contrast to TDS, the output signal of the FTIR spectrometer is proportional to the intensity of the FIR field. However, recent results have demonstrated [140] that the SNR of TDS is better than that of FTIR for frequencies in the range 10 GHz–4 THz. In this range the field amplitude SNR of THz TDS is 10^4 while that of FTIR is about 300. Beyond this frequency range (the FTIR method is able to work from FIR up to the visible spectral range), the SNR of FTIR is better. The SNR of TDS is drastically decreased when its bandwidth is increased up to 40 THz [141]. Both methods show a similar spectral resolution $\approx 0.1 \text{ cm}^{-1}$.

Thus, TDS is an extremely powerful method of spectroscopy, working at room temperature with an impressive sensitivity. TDS is performed in two steps. First, a reference signal $E_r(t)$ is detected in the absence of the sample. Then, a signal in the presence of the sample, $E_s(t)$, is detected. The transmission function of the TDS is given by

$$T(\omega) = F(E_s(t))/F(E_r(t)) = E_s(\omega)/E_r(\omega) = |T(\omega)| \exp[i\varphi(\omega)], \quad (44)$$

where $F(\dots)$ signifies the integral Fourier transform. The index of refraction of the sample $N = n + ik$ is related to the transmission function through the equation:

$$T(\omega) = 4N \exp[i\omega(N-1)d/c] \sum_{i=0}^P \{[(N-1)/(N+1)] \exp(i\omega N d/c)\}^{2i}, \quad (45)$$

where d is the thickness of the sample. Expression (45) is the transfer function resulting from the passage of the THz field through the sample, the THz field being reflected P times inside the sample. These repeated reflections inside the sample, which can be modeled as a Fabry–Perot-like effect, are seen in the time domain as distinct pulses accompanying the main time domain response. Thus, P is easily determined at least in the case of thick samples (see Fig. 41).

When $P = 0$, Eq. (45) allows a simply determination of the real and imaginary parts of the refractive index of the material as

$$|T(\omega)| = 2(n^2 + k^2)^{1/2} \exp(-\omega k d/c) / [(n+1)^2 + k^2], \quad (46a)$$

$$\varphi(\omega) = \omega(n-1)d/c + \arctan\{-k(n^2 + k^2 - 1)/[n(n+1)^2 + k^2(n+1)]\}. \quad (46b)$$

Solving the system formed by the last two equations we can extract the real and imaginary part of the index of refraction from the known amplitude and phase of the transmission function at a certain frequency. The procedure is repeated for any frequency with the bandwidth of the TDS system. Thus only two time-domain measurements are necessary to determine $T(\omega)$, from which the frequency behavior of the complex index of refraction of the material is determined. Both analytical methods [142] and numerical algorithms [143] are used to determine simultaneously

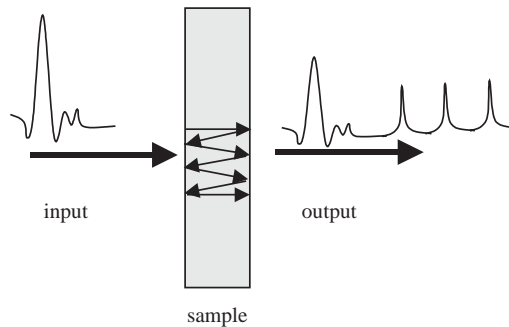


Fig. 41. THz TDS spectroscopy.

the index of refraction and the thickness of the sample, a procedure useful mainly for thin samples, where it is difficult to estimate the sample thickness.

In this manner, an impressive number of materials were measured in the THz domain, among them being semiconductors, dielectrics, ferroelectrics, high-temperature superconductors, gases and liquids. The study of each material type has conducted to an additional knowledge of other parameters. For example, in the case of semiconductors, carrier concentration and carrier mobility can also be determined. In the case of gases, each component of a gas mixture can be identified and in this way air composition monitoring becomes possible. A recent review about the applications of TDS in material characterization can be found in Ref. [144]. TDS is also an invaluable tool in the investigation of fundamental physical properties of semiconductors and heterostructures. In this respect, TDS was used extensively in the study of coherent phenomena, such as quantum interference of hole states, quantum interference of Landau levels, Bloch oscillations, THz emission by coherent photons, etc. The review of Roskos [145] is a valuable tool for those interested to find additional details, including TDS applications in atomic physics. Among the latest achievements of TDS in this area we mention the observation of dressing of bare particles inside a semiconductor plasma excited by an ultrafast optical pump (of about 10 fs) and probed by a THz pulse. The THz pulse probes the polarization of the electron–hole plasma formed by the fs optical pulse after a fixed time delay, then the THz output signal is recorded in time using a FS-EOS techniques. In this way, collective behaviors, such as Coulomb screening and plasmon scattering, were observed to occur at time delays of about 10^{-14} s, inversely equal to plasma oscillations [146,147].

The TDS was built due to a lack of continuous and tunable THz sources. Since there are now some THz sources (see Section 2.2), a new THz spectroscopy technique called CW THz spectroscopy (CWS) is being developed; for a review see Ref. [58]. Extremely high resolutions (linewidths less than 1 MHz) and high SNR ratio (better than 100:1) in narrow bandwidths are the main features of CWS, which surpass TDS. It was demonstrated that the CW power available in 1 MHz bandwidth is 10^4 times greater than that of a TDS system, and this happens when a photomixer delivers only 1 μ W output power at 1 THz. Tremendous results could be obtained if the photomixer power could be increased at 1 mW. The CW THz field was detected with either photoconductive or FS-EOS sampling techniques using as a gating signal the delayed optical signal excitation (see Eq. (26)) that contains the frequency difference of the two lasers and thus extends TDS detection techniques to CW. In the case of CW photoconductive sampling detection two identical photomixers were used, which form a transceiver configuration. The photomixer that plays the role of the detector was gated by a delayed version of the optical signal excitation. Both photomixers were excited by laser diodes, and the optical signal was carried out through optical fibers up to the photomixer surfaces [148]. It is important to note that THz CW detectors are also able to determine the amplitude and the phase of the transmitted THz signal. The amplitude is measured as the average output of the photomixer detector when the delay is changed and the phase is

determined measuring the change in paths between two consecutive zeros of the output fringes. A heterodyne receiver will offer even better performances.

Imaging of composite materials, such as biological tissues, boxes containing food, leaves, integrated circuits, bank notes, teeth, floppy disks, paintings, etc., reveals hidden details inside these materials due to the fact that the THz radiation penetrates non-metallic and non-polarizing materials such as semiconductors, plastics and textiles. The imaging techniques were a natural development of THz spectroscopy techniques. In the case of TDS, the object to be scanned is placed in the focal plane of the THz beam and is translated across the x - y plane for image acquisition, the THz intensity being recorded at each point. The image is then constructed pixel by pixel, and requires much time for completion. 2D THz intensity distributions can, however, be directly recorded using EO technique. In this case, a THz beam (pump) and a readout optical signal (probe), which probes the electric field distribution within the EO crystal, are applied to a ZnTe plate. The 2D THz field distribution is converted into a 2D optical intensity and is recorded by a CCD camera, after passing the optical readout through an analyzer [149].

CW imaging systems are expected to have better spatial resolutions and image qualities than the imaging systems based on ultrashort pulses. There are many THz review papers dedicated only to THz imaging. Two of them are in particular very appealing: Refs. [150,151].

There are other configurations that can be employed for THz spectroscopy or imaging, such as reflection configuration, differential TDS, or chirped probe THz pulse. Their performances are described in the references indicated above and in Refs. [152,153].

There are an increasing number of papers dealing with the imaging of biological tissues and genetics. It is worth mentioning what we can expect from THz imaging in comparison with X-ray imaging or X-ray tomography. X-rays can penetrate inside the body obtaining images of interior organs. However, no clear images are obtained for low-index materials. Thus, THz imaging is an additional investigation tool besides X-ray. However, THz radiation cannot penetrate deep inside the body due to the water content in any cell, and only skin, hair, teeth or dried biological samples can be investigated; this is a serious drawback for THz imaging. The spatial resolution of 0.3 mm is much worse compared to X-ray and it is another major drawback. However, the THz field is much less scattered, due to the much longer wavelength, allowing the visualization of objects hidden in granular materials (powders) [24]. THz beams are not harmful for living beings, while X-rays, which are ionizing radiations, become dangerous beyond a certain dose. Recently an entire special issue of *Physics in Medicine and Biology* (vol. 47, number 21, November 2002) was dedicated to biological imaging using THz techniques.

In genetics the first steps involving THz radiation have been already made. Label-free analysis of DNA, i.e. hybridization detection, was recently performed with a very high sensitivity, allowing the detection of a single base mutation of DNA molecules. The DNA sample is placed on a planar microstrip bandpass filter acting as a THz resonator and the genetic diagnostic is realized by monitoring the

transmission of the filter when DNA is denatured or hybridized. The changing of the resonance frequency of the filter allows a sensitivity up to a femtomol level [10].

Astronomy is a special area of THz applications. However, we will not review these applications here. Interested readers can consult Ref. [5] for a comprehensive review of this type of THz applications.

6. Conclusions

A simple inspection of the references shows that their large majority is not older than two years. This demonstrates how emerging the THz technology really is. The present THz technology is strongly dominated by ultrafast optical techniques from which THz emission or detection results as a down-conversion process, but these techniques are in serious competition with electronic techniques. These later techniques benefit from the most modern technologies developed in electronics, such as MEMS or nanotechnologies, having as an ultimate consequence a serious decrease of the costs of a THz system, a significant increase of the sensitivity and a large reproducibility. This is the only chance for THz technology to spread in industrial applications such as gas detection and air monitoring miniaturized systems, portable spectrometers, or medical tools. One of the largest markets in the world is the communication market. The development of optical communications at Terabits speeds will force the parallel development of specific THz modulators and detectors for optical signals. THz transistors switching 10^{12} times in a second are an achievable goal in a couple of years. THz communications are not developed at its full potential due to the high attenuation encountered in the THz range, but short-distance communications systems are still achievable.

The micro and nanotechnologies found numerous applications in the THz range. Devices with unprecedented performances can be built based on them. A must for the THz technology is a miniaturized THz tunable source and a THz amplifier. The development of THz transistors and THz multipliers will make this task realizable in a couple of years. However, only a robust presence in the communication and medical markets will turn THz into a mature technology. Some small companies in the THz area have already appeared in the last two years, most of them as spin-off companies of university departments. However, only the development of THz technology inside important companies will boost the THz technology from the academic level to industrial applications.

References

- [1] E.R. Brown, J.R. Söderström, C.D. Parker, L.J. Mahoney, K.M. Molvar, T.C. McGill, *Applied Physics Letters* 58 (1991) 2291–2293.
- [2] J. Nishizawa, P. Plotka, T. Kurabayashi, *IEEE Transactions on Electron Devices* 49 (2002) 1102–1111.
- [3] E. Alekseev, D. Pavlidis, *IEEE Microwave Technique and Techniques Symposium*, Boston, USA, 2000, pp. 1905–1909.

- [4] R. Köhler, A. Tredicucci, F. Beltram, H.E. Beere, E.H. Linfield, A. Gilles Davies, D.A. Ritchie, R.C. Iotti, F. Rossi, *Nature* 417 (2002) 156–159.
- [5] P.H. Siegel, *IEEE Transactions on Microwave Theory and Techniques* 50 (2002) 910–928.
- [6] B.I. Greene, J.F. Federici, D.R. Dykaar, R.R. Jones, P.H. Buksbaum, *Applied Physics Letters* 59 (1991) 893.
- [7] D. Grischkowsky, S. Keiding, M. van Exter, C. Fattinger, *Journal of Optical Society of America B* 7 (1990) 2006–2015.
- [8] J.W. Digby, C. McIntosh, G. Parkhurst, B.M. Towson, S. Hidjiloucas, J.W. Bowen, J.M. Chamberlain, R.D. Pollard, R.E. Milles, P. Steenson, L.S. Karatzas, N.J. Cronin, S.R. Davies, *IEEE Transactions on Microwave Theory and Techniques* 48 (2000) 1293–1302.
- [9] C. Mann, 30th European Microwave Conference, Paris, France, 2000, pp. 1–4.
- [10] M. Nagel, P. Haring Bolivar, M. Brucherseifer, H. Kurz, *Applied Physics Letters* 80 (2002) 154–156.
- [11] R. Chau, B. Doyle, J. Kavalieros, D. Barlage, A. Murthy, M. Doczy, R. Arghavani, S. Datta, International Conference on Solid State Devices and Materials, Nagoya, Japan, 2002, pp. 68–69.
- [12] D.D. Nolte, *Journal of Applied Physics* 85 (1999) 6259–6289.
- [13] G. Mourou, C.V. Stancampiano, A. Onetti, A. Orszag, *Applied Physics Letters* 39 (1981) 295–296.
- [14] D.H. Auston, K.P. Cheung, P.R. Smith, *Applied Physics Letters* 45 (1984) 284–286.
- [15] P.R. Smith, D.H. Auston, M.C. Nuss, *IEEE Journal of Quantum Electronics* 24 (1988) 255.
- [16] Z. Piao, M. Tani, K. Sakai, *Japanese Journal of Applied Physics* 39 (2000) 96–100.
- [17] D.B. Rutledge, S.E. Schwartz, A.T. Adams, *Infrared Physics* 18 (1978) 713–729.
- [18] G.M. Rebeiz, *Proceedings of IEEE* 80 (1992) 1748–1770.
- [19] T.M. Weller, L.P. Katechi, G.M. Rebeiz, *IEEE Transactions on Antennas and Propagation* 43 (1995) 1423–1428.
- [20] D.W. van der Weide, *Journal of Optical Society of America B* 11 (1994) 2553–2560.
- [21] K.S. Yngvesson, D.H. Scaubert, T.L. Korzeniowski, E.L. Kolberg, T. Thungren, J.F. Johansson, *IEEE Transactions on Antennas and Propagation* 33 (1985) 1392–1400.
- [22] Y. Cai, I. Brener, J. Lopata, L. Pfeiffer, J. Federici, *Applied Physics Letters* 71 (1997) 2076–2078.
- [23] N. Sarukura, H. Ohtake, S. Izumida, Z. Liu, *Journal of Applied Physics Letters* 84 (1998) 654–656.
- [24] M. Tani, M. Herrmann, K. Sakai, *Measurement Science and Technology* 13 (2002) 1739–1745.
- [25] D.F. Filipovic, S.S. Gearhart, G.M. Rebeiz, *IEEE Transactions on Microwave Theory and Techniques* 41 (1993) 1738–1749.
- [26] D.F. Filipovic, G.P. Gauthier, S. Raman, G.M. Rebeiz, *IEEE Transactions on Antennas and Propagation* 45 (1997) 760–766.
- [27] J. van Rudd, D.M. Mittlemann, *Journal of Optical Society of America B* 19 (2002) 319–329.
- [28] N.M. Froberg, B.B. Hu, X.C. Zhang, D.H. Auston, *IEEE Transactions on Quantum Electronics* 28 (1992) 2291–2301.
- [29] T. Pfeiffer, H.M. Heiliger, E.S. von Kamienski, H.G. Roskos, H. Kurtz, *Journal on Optical Society of America B* 11 (1994) 2547–2552.
- [30] R.K. Lai, J.R. Hwang T.B. Noriss, J.F. Whiteker, *Applied Physics Letters* 72 (1998) 3100–3102.
- [31] O. Mitrofanov, I. Brener, M.C. Wanke, R.R. Ruel, J.D. Wynn, A.J. Bruce, J. Federici, *Applied Physics Letters* 77 (2000) 591–593.
- [32] M. Tani, M. Watanabe, K. Sakai, *Electronics Letters* 38 (2002) 5–6.
- [33] D. Grischkowsky, M.B. Ketchen, C.C. Chi, I. N. Dulling III, N.J. Halas, J.M. Halbout, P.G. May, *IEEE Journal of Quantum Electronics* 24 (1988) 221–225.
- [34] N. Katzenellenbogen, D. Grischkowsky, *Applied Physics Letters* 58 (1991) 222–224.
- [35] D. Grischkowsky, *IEEE Journal of Selected Topics in Quantum Electronics* 6 (2000) 1122–1135.
- [36] P.K. Benicewicz, J.P. Roberts, A.J. Taylor, *Journal of Optical Society America B* 11 (1994) 2533–2546.
- [37] J.T. Darrow, X.C. Zhang, D.H. Auston, *IEEE Journal of Quantum Electronics* 28 (1992) 1607–1616.
- [38] S.G. Park, A.M. Weiner, M.R. Melloch, C.W. Seiders, A.J. Taylor, *IEEE Journal of Quantum Electronics* 35 (1999) 1257–1268.

- [39] J.F. Holzman, F.E. Vermeulen, A.Y. Elezzabi, *IEEE Journal of Quantum Electronics* 36 (2000) 130–136.
- [40] D. Dragoman, M. Dragoman, *Progress in Quantum Electronics* 25 (2001) 229–290.
- [41] X.C. Zhang, B.B. Hu, J.T. Darrow, D.H. Auston, *Applied Physics Letters* 56 (1990) 1011–1013.
- [42] X.C. Zhang, J.T. Darrow, B.B. Hu, D.H. Auston, M.T. Schmidt, P. Tham, E.S. Yang, *Applied Physics Letters* 56 (1990) 2228–2230.
- [43] X.C. Zhang, B.B. Hu, S.H. Xin, D.H. Auston, *Applied Physics Letters* 57 (1990) 753–755.
- [44] D. Côte, J.M. Fraser, M. de Camp, P.H. Bucksbaum, H.M. van Driel, *Applied Physics Letters* 75 (1999) 3959–3961.
- [45] D.H. Auston, M.C. Nuss, *IEEE Journal of Quantum Electronics* 24 (1988) 184–197.
- [46] Q. Wu, X.C. Zhang, *IEEE Journal of Selected Topics in Quantum Electronics* 2 (1996) 693–700.
- [47] A. Nahata, *Optics Letters* 26 (2001) 385–387.
- [48] A. Bonvalet, M. Joffre, J.L. Martin, A. Migus, *Applied Physics Letters* 67 (1995) 2907–2909.
- [49] A. Rice, Y. Jin, X.F. Ma, X.C. Zhang, D. Bliss, J. Larkin, M. Alexander, *Applied Physics Letters* 64 (1994) 1324–1326.
- [50] A. Nahata, A.S. Welington, T.F. Heinz, *Applied Physics Letters* 69 (1996) 2321–2323.
- [51] A.S. Nikogossian, E.M. Laziev, A.A. Hakhomian, N.G. Pogossyan, *The Digest of the 25th International Conference on Infrared and Millimeter Waves*, Beijing, China, 2000, pp. 65–66.
- [52] D. van der Weide, *Applied Physics Letters* 65 (1994) 881–883.
- [53] J.S. Bostak, D.W. van der Weide, D.M. Bloom, B.A. Auld, *Journal of Optical Society of America B* 11 (1994) 2561–2565.
- [54] M.J.W. Rodwell, S.T. Allen, R.T. Yu, M.G. Case, U. Bhattacharya, M. Reddy, E. Carman, M. Kamegawa, Y. Konishi, J. Puhl, R. Pullera, *Proceedings of IEEE* 82 (1994) 1037–1059.
- [55] M. Dragoman, D. Dragoman, An overview of nonlinear microwave and millimeter wave generation in magnetic, acoustic and electromagnetic distributed nonlinear physical systems, in: R. Marcelli, S. Nikitov (Eds.), *Nonlinear Microwave Signal Processing: Towards a New range of Devices*, NATO ASI Series, Vol. 20, 1996, pp. 13–43.
- [56] X. Orlos, F. Martin, *Journal of Applied Physics* 90 (2001) 2595–2600.
- [57] M.C. Gaidis, H.M. Pickett, C.D. Smith, S.C. Martin, P.R. Smith, P.H. Siegel, *IEEE Transactions on Microwave Theory and Techniques* 48 (2000) 733–739.
- [58] K.J. Siebert, H. Quast, H.G. Roskos, *Perspectives of continuous-wave optoelectronic THz imaging*, in: R.E. Miles (Ed.), *Terahertz Sources and Systems*, Kluwer Academic, Dordrecht, 2001, pp. 127–143.
- [59] S.M. Duffy, S. Verghese, K.A. McIntosh, *Photomixers for Continuous-Wave Terahertz Radiation*, in: D. Mittleman (Ed.), *Sensing with Terahertz Radiation*, Springer, Berlin, 2002.
- [60] E.R. Brown, F.W. Smith, K.A. McIntosh, *Journal of Applied Physics* 73 (1993) 1480–1484.
- [61] K.A. McIntosh, E.R. Brown, K.B. Nichols, O.B. McMahon, W.F. DiNatale, *Applied Physics Letters* 69 (1996) 3632–3634.
- [62] S. Matsuura, M. Tani, K. Sakai, *Applied Physics Letters* 70 (1997) 559–561.
- [63] S. Verghese, K.A. McIntosh, E.R. Brown, *IEEE Transactions on Microwave Theory and Techniques* 45 (1997) 1301–1309.
- [64] S.M. Duffy, S. Verghese, K.A. McIntosh, A. Jackson, A.C. Gossard, S. Matsuura, *IEEE Transactions on Microwave Theory and Techniques* 49 (2001) 1032–1038.
- [65] S. Verghese, K.A. McIntosh, E.R. Brown, *Applied Physics Letters* 71 (1997b) 2743–2745.
- [66] E.R. Brown, *Applied Physics Letters* 75 (1999) 769–771.
- [67] C. Kadow, A.W. Jackson, A.C. Gossard, S. Matsuura, G.A. Blake, *Applied Physics Letters* 76 (2000) 3510–3512.
- [68] M. Eckardt, A. Schwanhäuß, F. Renner, L. Robledo, A. Friedrich, P. Pohl, P. Kiesel, S. Maltzer, G.H. Döhler, D. Driscoll, M. Hanson, A.C. Gossard, *Third Symposium on Non-Stoichiometric III–V Compounds*, Erlangen, Germany, 2001.
- [69] E. Peytavit, S. Arscott, D. Lippens, G. Mouret, S. Matton, P. Masselin, R. Bocquet, J.F. Lamplin, L. Desplanque, F. Mollot, *Applied Physics Letters* 81 (2002) 1174.

- [70] S. Matsura, P. Chen, G.A. Blake, J.C. Pearson, H.M. Pickett, *IEEE Transactions on Microwave and Techniques* 48 (2000) 380–387.
- [71] D. Pasqualini, A. Neto, R.A. Wyss, *Microwave and Optical Letters* 33 (2002) 430–435.
- [72] K. Kourogi, B. Widiyatmoko, M. Ohtsu, *IEEE Photonics Technology Letters* 8 (1995) 560–562.
- [73] K. Siebert, F. Siebe, M. Thomson, J.Z. Baghbi, R. Leonhardt, H. Roskos, *Proceedings of SPIE* 3828 (1999) 234–243.
- [74] O. Morikawa, M. Tonouchi, M. Tani, K. Sakai, M. Hangyo, *Japan Journal of Applied Physics* 38 (1999) 1388–1389.
- [75] L. Chusseau, G. Almuneau, L.A. Coldren, A. Huntington, D. Gasquet, *Proceedings of IEE J* 149 (2002) 88–92.
- [76] J.-I. Shikata, K. Kawase, K.-I. Karino, T. Taniuchi, H. Ito, *IEEE Transactions on Microwave Theory and Techniques* 48 (2000) 653–661.
- [77] K. Kawase, J.I. Shikata, H. Ito, *Journal of Applied Physics D* 34 (2001) R1–R14.
- [78] H. Eisele, A. Rydberg, G.I. Haddad, *IEEE Transactions on Microwaves and Techniques* 48 (2000) 626–630.
- [79] H. Eisele, *Proceedings of the 10th IEEE International Conference on Terahertz Electronics*, Cambridge, UK, 2002, pp. 13–18.
- [80] Z.S. Gribnikov, N.Z. Vagidov, V.V. Mitin, G.I. Haddad, *Journal of Applied Physics* 93 (2003) 5435–5446.
- [81] M. Saglam, B. Schumann, V. Müllerwiebus, A. Megej, U. Auer, M. Rodrigues-Gironés, R. Jurdaschke, F.J. Tegude, H.L. Hartnagel, *Electronics Letters* 38 (2002) 657–658.
- [82] S.A. Mass, *Nonlinear Microwave Circuits*, Artech House, London, 1988.
- [83] E.I. Kolberg, J. Stake, L. Dillner, *Philosophical Transactions of the Royal Society A* 354 (1996) 2383–2398.
- [84] H. Hartnagel, 32nd European Microwave Conference, 2002, Milano, Italy, pp. 249–252.
- [85] A. Maestrini, J. Bruston, D. Pukala, S. Martin, I. Mehdi, *IEEE International Symposium Digest*, Phoenix, USA, 2001, pp. 20–25.
- [86] F. Maiwald, S. Martin, J. Bruston, A. Maestrini, T. Crawford, P.H. Siegel, *IEEE International Symposium Digest*, Phoenix, USA, 2001, pp. 1637–1640.
- [87] J.N. Hovenier, M.C. Diaz, T.O. Klaassen, W.T. Wenckebach, A.V. Muravjov, S.V. Pavlov, V.N. Shastin, *IEEE Transactions on Microwave Theory and Techniques* 48 (2000) 670–676.
- [88] R. Kazarionov, R.A. Suris, *Soviet Physics Semiconductors* 5 (1971) 707–709.
- [89] F. Capasso, R. Paiella, R. Martini, R. Colombelli, C. Gmachl, T.L. Myers, M.S. Taubman, R.M. Williams, C.G. Bethea, K. Unterrainer, H.Y. Hwang, D.L. Sivco, A.Y. Cho, A.M. Sergent, H.C. Liu, E.A. Whittaker, *IEEE Journal of Quantum Electronics* 38 (2002) 511–532.
- [90] J. Faist, D. Hofstetter, M. Beck, T. Aellen, M. Rochat, S. Blaser, *IEEE Journal of Quantum Electronics* 38 (2002) 533–546.
- [91] D. Dragoman, M. Dragoman, *Advanced Optoelectronic Devices*, Springer, Berlin, 1999.
- [92] M. Rocahat, L. Ajili, H. Willenberg, J. Faist, H. Beere, G. Davies, E. Linfield, D. Ritchie, *Applied Physics Letters* 81 (2002) 1381–1383.
- [93] L. Fridman, G. Sun, R.A. Soref, *Applied Physics Letters* 78 (2001) 401–403.
- [94] G. Sun, R.A. Soref, J.B. Kurgin, *IEEE Journal of Selected Topics in Quantum Electronics* 7 (2001) 376–380.
- [95] P. Kinsler, P. Harrison, R.W. Kelsall, *Journal of Applied Physics* 85 (1999) 23–28.
- [96] J.B. Kurgin, K.L. Wang, *Superlattices and Microstructures* 22 (1997) 551–557.
- [97] S. Starikov, P. Shiktorov, V. Gruzinskis, L. Reggiani, L. Varani, J.C. Vassiere, J.H. Zhao, *Transactions on IEEE Electron Devices* (2001) 438–443.
- [98] H.G. Roskos, M.C. Nuss, J. Shah, K. Leo, D.A.B. Miller, A.M. Fox, S. Schmitt-Rink, K. Köhler, *Physical Review Letters* 68 (1992) 2216–2219.
- [99] M.S.C. Luo, S.L. Chuang, P.C.M. Planken, I. Brener, H.G. Roskos, M.C. Nuss, *IEEE Journal of Quantum Electronics* 30 (1994) 1478–1488.
- [100] C. Waschke, H.G. Roskos, R. Schwedler, K. Leo, H. Kurtz, K. Köhler, *Physical Review Letter* 70 (1993) 3222–3319.

- [101] H.G. Roskos, R. Martini, G. Klose, F. Wolter, C. Schwarz, H. Kurz, Tunable coherent THz radiation pulses from optically excited Bloch oscillations, in: J.M. Chamberlain, R.E. Miles (Eds.), *New Directions in Terahertz Technology*, NATO ASI Science Series E, Vol. 334, Kluwer, Dordrecht, 1997, pp. 369–375.
- [102] D.A. Ryndyk, N.V. Demaria, J. Keller, E. Schomberg, *Physical Review B* 67 (2003) 0033305.
- [103] M.I. Dyakonov, M.S. Shur, *IEEE Transactions on Electron Devices* 43 (1996) 380–387.
- [104] M.I. Dyakonov, M.S. Shur, *IEEE Transactions on Electron Devices* 43 (1996) 1640–1645.
- [105] V. Ryzhii, M. Shur, *Semiconductor Science and Technology* 17 (2002) 1168–1171.
- [106] J. Mateos, B.G. Vasallo, D. Pardo, T. Gonzales, J.S. Galloo, Y. Roelens, A. Cappy, *Nanotechnology* 14 (2003) 117–122.
- [107] S. Grafström, *Journal of Applied Physics* 91 (2002) 1717–1753.
- [108] A. Mayer, J.P. Vigneron, *Physical Review B* 62 (2000) 16138–16145.
- [109] A.A. Odintsov, *Physical Review Letters* 85 (2000) 150–153.
- [110] A.S. Maksimenko, G.Ya. Slepyan, *Physical Review Letters* 85 (2000) 362–365.
- [111] F. Léonard, J. Tersoff, *Physical Review Letters* 85 (2000) 4767–4770.
- [112] H.M. Manohara, P.H. Sigel, C. Marrese, B. Chang, J. Xu, Far IR, submillimeter and millimeter detector technology Workshop, Monterey, USA, 2002.
- [113] D. Dragoman, M. Dragoman, *IEEE Journal of Quantum Electronics* 32 (1996) 1150–1154.
- [114] P.F. Goldsmith, *Proceeding of IEEE* 80 (1992) 1729–1747.
- [115] J.A. Arnaud, *Beam and Fiber Optics*, Academic Press, New York, 1976.
- [116] D.H. Martin, J.W. Bowen, *IEEE Transactions on Microwave Theory and Techniques* 41 (1993) 1676–1690.
- [117] M.E. MacDonanld, A. Alexandrian, R.A. York, Z. Popovic, E.N. Grossmann, *IEEE Transactions on Microwave Theory and Techniques* 48 (2000) 712–718.
- [118] D. Rutledge, *IEEE Microwave Symposium*, 1996, San Francisco, 1889–1892.
- [119] L.P. Katehi, *Proceedings of IEEE* 80 (1992) 1771–1787.
- [120] V.M. Lubecke, K. Mizuno, G.M. Rebeiz, *IEEE Transactions on Microwave Theory and Techniques* 44 (1998) 1821–1831.
- [121] S.P. Jamison, R.W. McGowan, D. Grischkowsky, *Applied Physics Letters* 76 (2000) 1987–1989.
- [122] R.W. McGowan, G. Gallot, D. Grischkowsky, *Optics Letters* 24 (2000) 1431–1433.
- [123] R. Mendis, D. Grischkowsky, *Optics Letters* 26 (2001) 846–848.
- [124] S.G. Park, M.R. Melloch, A.M. Weiner, *Applied Physics Letters* 73 (1998) 3184–3186.
- [125] C. Winnewisser, P.U. Jepsen, M. Schall, V. Schyja, H. Helm, *Applied Physics Letters* 70 (1997) 3059–3071.
- [126] Y. Cai, I. Brener, J. Lopata, J. Wynn, L. Pfeiffer, J.B. Stark, Q. Wu, X.C. Zhang, J.F. Federici, *Applied Physics Letters* 73 (1998) 444–446.
- [127] P.Y. Han, X.C. Zhang, *Applied Physics Letters* 73 (1998) 3049–3051.
- [128] A. Jelenski, A. Grös, V. Krozer, H.L. Hartnagel, *IEEE Transactions on Microwave Theory and Techniques* 41 (1993) 549–557.
- [129] P.H. Siegel, R.P. Smith, M.C. Gaidis, S.C. Martin, *IEEE Transactions on Microwave Theory and Techniques* 47 (1999) 596–604.
- [130] E. Gerecht, C.F. Musante, Y. Zhuang, K.S. Yngvesson, T. Goyette, J.C. Dickinson, J. Waldman, P.A. Yagoubov, G.N. Gol'tsman, B.M. Voronov, E.M. Gershenzon, *IEEE Transactions on Microwave Theory and Techniques* 47 (1999) 2519–2527.
- [131] J. Kawamura, R. Blundell, C.Y.E. Tong, D. Cosmo Popa, T.R. Hunter, S.C. Paine, F. Patt, G.N. Gol'tsman, S. Cherednichenko, B.M. Voronov, E.M. Gershenzon, *IEEE Transactions on Microwave Theory and Techniques* 48 (2000) 683–689.
- [132] P. Focardi, A. Neto, W.R. McGrath, *IEEE Transactions on Microwave Theory and Techniques* 50 (2002) 2374–2383.
- [133] A.D. Semenov, G.N. Gol'tsman, R. Sobolewski, *Laboratory Laser Energetics Review* 87 (2001) 134–152.
- [134] C.C. Ling, J.C. Landry, H. Daveé, G. Chin, G.M. Rebeiz, *IEEE Transactions on Microwave Theory and Techniques* 42 (1994) 758–760.

- [135] D. Dragoman, M. Dragoman, *Applied Physics Letters* 79 (2001) 581–583.
- [136] K.S. Yngvegsson, *Applied Physics Letters* 76 (2000) 777–779.
- [137] J.Q. Lü, M. Shur, *Applied Physics Letters* 78 (2001) 2587–2588.
- [138] M. Ryzhii, M.W. Willander, I. Khmyrova, V. Ryzhii, *Journal of Applied Physics* 84 (1998) 6419–6425.
- [139] O. Astafiev, S. Komiyama, T. Kutsuwa, *Applied Physics Letters* (2001) 1199–1200.
- [140] P.Y. Han, M. Tani, M. Usami, S. Kono, R. Kersing, X.C. Zhang, *Journal of Applied Physics* 89 (2001) 2357–2359.
- [141] Q. Wu, X.C. Zhang, *Applied Physics Letters* (1997) 1285–1287.
- [142] L. Duvallaret, F. Garet, J.L. Coutaz, *IEEE Journal of Selected Topics in Quantum Electronics* 2 (1996) 739–746.
- [143] T.D. Dorney, R.G. Baraniuk, D.M. Mittleman, *Journal of Optical Society America A* 18 (2001) 1562–1571.
- [144] B. Ferguson, X.C. Zhang, *Nature Materials* 1 (2002) 26–33.
- [145] H.G. Roskos, *Physica Scripta T* 86 (2000) 51–54.
- [146] H. Haug, *Nature* 414 (2001) 261.
- [147] R. Huber, F. Tauser, A. Brodschheim, M. Bichler, G. Abstreiter, L.A. Leitenstorfer, *Nature* 414 (2001) 286–289.
- [148] S. Verghese, K.A. McIntosh, S. Calawa, W.F. Dinatale, E.K. Duerr, K.A. Molvar, *Applied Physics Letters* 73 (1998) 3824–3826.
- [149] Z. Jiang, X.C. Zhang, *IEEE Transactions on Microwave Theory and Techniques* 47 (1999) 2644–2650.
- [150] D.M. Mittleman, M. Gupta, R. Neelamani, R.G. Baraniuk, J.V. Rudd, M. Koch, *Applied Physics B* 68 (1999) 1085–1094.
- [151] S. Mickan, D. Abbott, J. Munch, X.C. Zhang, T. van Dorn, *Microelectronics Journal* 31 (2000) 503–514.
- [152] S. Mickan, K. S. Lee, T.M. Lu, J. Munch, D. Abbott, X.C. Zhang, *Microelectronics Journal* 33 (2002) 1033–1042.
- [153] B. Ferguson, S. Wang, D. Abbott, D. Gray, D. Abbot, X.C. Zhang, *Microelectronics Journal* 33 (2002) 1043–1051.